Additive Manufacturing 105 (2025) 104788

Contents lists available at ScienceDirect

Additive Manufacturing

journal homepage: www.elsevier.com/locate/addma

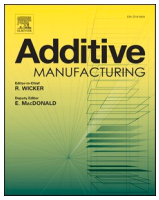

# On the viability of in-situ alloyed Ti-1Fe as a strong and ductile alternative to Ti-6Al-4V for laser-based powder bed fusion

Jeff Huang [a,b,*], Ammarueda Issariyapat [a,**], Shota Kariya [a], Junko Umeda [a], Katsuyoshi Kondoh [a]

[a] Joining and Welding Research Institute, The University of Osaka, 11-1 Mihogaoka, Ibaraki, Osaka 567-0047, Japan
[b] Graduate School of Engineering, The University of Osaka, 2-1 Yamadaoka, Suita, Osaka 565-0871, Japan

ARTICLE INFO

*Keywords:*
Titanium
Laser powder bed fusion
In-situ alloying
Microstructures
Mechanical Properties

ABSTRACT

Developments in the additive manufacturing (AM) of titanium have historically centred around the market-leading Ti-6Al-4V alloy, with many studies aimed at adapting the seventy-year-old composition for newer AM processes such as laser-based powder bed fusion (PBF-LB/M). Amongst these studies, PBF-LB/M Ti-6Al-4V is usually shown to be remarkably strong (with gigapascal ultimate tensile strengths) and moderately ductile (if defect free), because of the ultra-fine martensitic α/α' microstructures produced under the rapid cooling conditions of PBF-LB/M. However, despite these acceptable properties, the use of Ti-6Al-4V in AM fundamentally contradicts the original intention behind the design of this alloy composition, which relies on rare and expensive vanadium solutes to promote α+ β microstructures for good wrought-forming properties. In essence, neither the intended microstructures, nor the intended properties are relevant or compatible with near-net-shape AM processes. Therefore, it seems natural to question the strict adherence to conventional alloys in PBF-LB/M. In search of alternatives, the present study attempts to replicate the microstructures and properties of PBF-LB/M Ti-6Al-4V using the cheaper and leaner composition of Ti-1Fe prepared by in-situ alloying (i.e. from mixed elemental feedstocks). Both fine and coarse Fe particles were investigated to identify optimal feedstock characteristics and build parameters. In homogeneously mixed samples prepared from fine Fe particles at higher energy densities, similar microstructures to Ti-6Al-4V were successfully obtained, with corresponding tensile properties that exceed the performance requirements of ASTM F2924 (950 MPa yield strength, 12 % fracture strain). A theoretical analysis of strengthening mechanisms revealed significant contributions from grain refinement effects, dislocation hardening, and solid solution strengthening by oxygen and nitrogen interstitials. With these findings, we report for the first time the prerequisite conditions for obtaining strong and ductile tensile properties from as-built, in-situ alloyed Ti-1Fe as a potential low-cost alternative to Ti-6Al-4V for PBF-LB/M, and the problems that may occur with sub-optimal processing.

## 1. Introduction

In the past decade, near-net-shape additive manufacturing (AM) of titanium (Ti) alloys has garnered considerable attention as an attractive means of overcoming their high costs and low machinability. In particular, high-resolution AM techniques such as laser-based powder bed fusion of metals (PBF-LB/M) appear to be a ideal solution for manufacturing complex Ti products like implantable prostheses, and aerospace components with greater geometric freedom and less material wastage [1,2]. However, the demand and desire to adapt Ti to AM processes has substantially outpaced the metallurgical development of process-suitable alloy compositions, and as a result, it has unfortunately become common practice to directly implement conventional Ti alloy compositions without adequate consideration of the complex thermal histories found in the new processes. This regrettable disconnect between alloy design, processing conditions, and microstructure development has left some significant shortcomings in terms of cost-efficiency and sustainability.

For instance, the widely used Ti-6Al-4V alloy (ASTM Grade 5) is reported to deviate substantially from its intended wrought

* Corresponding author at: Joining and Welding Research Institute, The University of Osaka, 11-1 Mihogaoka, Ibaraki, Osaka 567-0047, Japan.
** Corresponding author.
*E-mail addresses:* j-huang.jwri@osaka-u.ac.jp (J. Huang), i.ammarueda.jwri@osaka-u.ac.jp (A. Issariyapat).

https://doi.org/10.1016/j.addma.2025.104788
Received 26 July 2024; Received in revised form 1 April 2025; Accepted 12 April 2025
Available online 14 April 2025

microstructures when prepared by PBF-LB/M. Instead of dual-phase microstructures with balanced strength and ductility (supported by wrought-processed mixtures of the hexagonal close packed (HCP) α phase and the body centred cubic (BCC) β phase [3]), PBF-LB/M Ti-6Al-4V usually presents hard and brittle martensitic microstructures consisting of ultra-fine α/α' plates, which develop as a result of the abnormally high cooling rates of the process (in the range of $10^4$–$10^6$ K/s) [4]. While there have been contrived attempts to post heat-treat these microstructures into lamellar α+ β for a more acceptable balance of strength and ductility (usually to a minimum fracture strain of 10 % as specified in ASTM F2924) [5–7], the optimal microstructures and properties remain impossible to obtain as near-net-shape parts are fundamentally incompatible with the necessary wrought processing. This contradiction is particularly concerning considering the rare and expensive vanadium (V) is explicitly included to stabilise the β phase, which is mostly absent from as-built microstructures, and is slow forming on heat-treatment due to the relatively slow diffusion of V [8].

Despite this, a substantial body of research has been developed around PBF-LB/M Ti-6Al-4V, and it naturally serves as an indispensable starting point and benchmark for any reconsideration of Ti alloy design for AM. In PBF-LB/M Ti-6Al-4V, the concentration of V is understood to govern the kinetics of the martensitic β→α/α' transformation in Ti alloys [9]. Thus, V and other β-stabilising elements can still be expected to exert a strong influence over the microstructure despite not fully stabilising the β phase. From this viewpoint, it appears possible to obtain a better balance of strength and ductility in microstructures similar to PBF-LB/M Ti-6Al-4V by considering alternate compositions of similar β stability and lower solute concentration (i.e., by balancing the increased grain refinement effects of the martensitic microstructures with reduced solid solution strengthening). Such compositions would mitigate the need for extensive post-treatments in attaining optimal properties, while also eliminating the costly inclusion of V.

To this end, iron (Fe) is an attractive element of study, with about four times the β stabilisation potential of V by measure of the Mo equivalency [10]. This means Fe can produce similar levels of β stabilisation at a quarter of the concentration of V (by weight). Such behaviour allows the cheap and abundant Fe to serve as an effective substitute for V in producing ultra-fine microstructures without producing excessive solution strengthening. Moreover, Ti-Fe based alloys have been affirmed to exhibit excellent corrosion resistance [11,12]. This is highly attractive for common AM components such as heat exchangers and biomedical implants. Additionally, Fe is a common contaminant in the refinement of Ti by the Kroll process, which has a reported 10–20 % scrap rate of Fe enriched off-grade waste (diffusive pick-up from contact with steel container walls) [13]. From this perspective, atomisation of these scraps and mixing them into AM feedstock material presents an attractive solution towards creating a circular economy around 'dirty' Ti-alloys [14,15]. However, the implementation of such a strategy requires a deeper understanding of how the Ti-Fe system behaves under AM conditions, especially with regards to intrinsic heterogeneities in the feedstock.

Herein, a lean binary composition of Ti-1Fe (wt%) is investigated as a potential alternative to Ti-6Al-4V in PBF-LB/M in terms of quasi-static tensile performance. For the first time, both compositions are equitably compared using identical PBF-LB/M conditions to evaluate the merits of without any biases or uncertainties from different testing equipment. This composition was selected based on the recent findings of Sandlöbes et al. [16], which report excellent mechanical properties in martensitic Ti-1Fe prepared by hot rolling and water quenching from the β-phase region. Amongst conventional processes, this processing route is the most similar to PBF-LB/M, suggesting this composition may be suitably adapted to AM. Recently, this idea was affirmed in a short communication from Liu et al. [17], which reports strong and ductile Ti-1Fe prepared by PBF-LB/M from mixed elemental feedstocks (in-situ alloying). However, their study is narrowly focused on investigating deformation mechanisms and does not investigate the application and mechanics of the in-situ alloying process used in their study. Considering the well-known complexity of blended elemental approaches in general, and in-situ alloying in particular, there remains a large gap in the understanding towards strategic development and application of this method and material in AM.

To partially address this gap in knowledge, the present work systematically investigates the influences of feedstocks and build parameters on the in-situ alloying behaviour of Ti-1Fe by PBF-LB/M to provide novel insight into the response of system to AM specific mechanisms. Specifically, the present study aims to address the optimisation of feedstock characteristics and build parameters towards processibility, porosity mitigation and obtaining high as-built tensile performance. For the first time, both coarse and fine Fe powders were evaluated as potential pre-cursors for alloy preparation, simulating heterogeneities that may be present in recycled Ti scrap; while a wide range of building parameters are investigated to study their influence on the defect structure, microstructure, and mechanical properties of the produced materials. The produced alloys are also compared with Ti-6Al-4V prepared under similar conditions from pre-alloyed powder, revealing the necessary conditions to obtain comparable performance in Ti-1Fe. Finally, the results are verified and clarified in a breakdown of theoretical strengthening mechanisms. The novel findings of this work serve as an informative and prerequisite foundation for further studies into the effects of post-heat treatments (including stress-relieving), fatigue, anisotropy, residual stresses and surface quality, which are all important aspects towards the development of this material for real-world AM applications.

## 2. Materials and methods

### 2.1. Feedstock preparation

Ti-1Fe feedstocks were prepared by mechanically mixing 1 wt% of Fe powder into a gas-atomised CP-Ti powder with spheroidal morphology (TILOP-45, Osaka Titanium). To investigate the influence of particle size on in-situ alloying dynamics, a fine Fe powder of ~5 μm (FEE16PB, Kojundo Chemical) was compared to a coarser Fe powder of ~25 μm (300 M, Kobe Steel, pre-sieved <45 μm mesh). The feedstocks containing fine and coarse Fe, and the respective PBF-LB/M samples prepared from them are henceforth referred to as Ti-1Fe(F) and Ti-1Fe(C), respectively. Mixing was performed by rocking mill (AV-2, Asahi Rika) in 500 g batches for 1 h at a setting of 60 Hz. To promote mixing, ø5 mm zirconia balls were added to each mixture at a ball-to-powder weight ratio of 1:10. Pre-alloyed Ti-6Al-4V (TILOP64–45, Osaka Titanium) was also used in as-received condition as a feedstock for reference Ti-6Al-4V samples. The particle size characteristics of as-received and mixed powders were analysed by laser diffraction analysis (LA-950, HORIBA). Oxygen (O), nitrogen (N), and hydrogen (H) contents in the powders and built materials were evaluated by inert gas fusion analysis (ONH, EMGA-830, HORIBA).

### 2.2. Test coupon fabrication

The prepared feedstocks were consolidated into rectangular test coupons (10 mm × 10 mm × 60 mm, Fig. 1b) using a commercial laser powder bed fusion system (TruPrint 1000, TRUMPF). This system was equipped with a fibre laser (wavelength: 1070 nm) focused to a spot of 30 μm in diameter. Building was conducted in a circulated argon atmosphere, with oxygen content in the circulation system maintained below 100 ppm. A chessboard scan strategy (Fig. 1a) was used to minimise the accumulation of residual stresses [18], with scanning directions (*X', Y'*) oriented at a 45° offset to the edges of the rectangular test coupons (*X, Y*). Individual chessboard squares were 3.96 mm × 3.96 mm in size, with a pattern shift of 2.73 mm and 3.22 mm in the *X'* and *Y'* directions respectively on subsequent layers. Each square was scanned with unconnected bi-directional hatching, with a 90° rotation

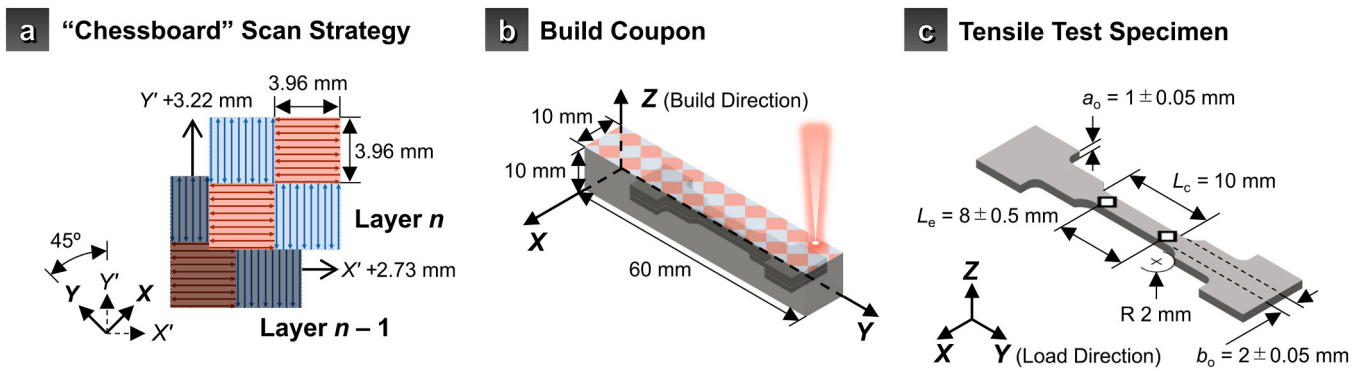


**Fig. 1.** Schematics of (a) "chessboard" PBF-LB/M scan-strategy, (b) test coupon geometry and (c) tensile-test specimen geometry used in the present study.

in scan direction between adjacent squares (i.e. alternating between *X'-X'* and *Y'-Y'*). Test coupons were built directly onto a pure-Ti substrate, using the build parameters in Table 1. Further in-text references to specific build parameters will follow the notation of the volumetric energy density ($E_V$) scalar followed by a hatch spacing ($h$) suffix, with '-S' for standard (110 μm) and '-W' for wide (150 μm). For example, the parameter of $E_V = 180$ Jmm$^{-3}$ at $h = 150$ μm is referred to as 180-W in the upcoming discussions.

### 2.3. Characterisation

In preparation for microscopy, cross sections of built samples were prepared by planar grinding with silicon carbide paper followed by a final polish using a 5:1 mixture of colloidal silica suspension and hydrogen peroxide (30 % concentration). Powder morphologies and built microstructures were characterised by scanning electron microscopy (SEM, JSM-7100F, JEOL), with simultaneous elemental distribution mapping by energy-dispersive X-ray spectroscopy (EDS, JED-2300, JEOL). Local Fe concentrations were quantified from spectral data using by the ZAF correction method in the built-in software (Analysis Station, JEOL). Meanwhile, overall concentrations of Al, V and Fe in the built samples were analysed by inductively coupled plasma emission spectrometry (ICP-OES, ICPS-8100, Shimadzu); representative samples ($n = 2$, ~0.25 g each) were sliced along the full height of each test coupon and extracted close to the centre of the test coupon (near the gauge sections of tensile specimens). Quantitative pore analysis was conducted with the PoreSpy toolkit for Python [19] using light microscope images (LM, DSX-M, Olympus). Phase distributions and grain orientations in the built microstructures were characterised by electron backscatter diffraction analysis (EBSD), using patterns collected at a working distance of 20 mm, tilt of 70°, and accelerating voltage of 15 kV (Hikari, EDAX).

To account for the large mismatch between prior-β and final α/α' grain sizes, EBSD patterns were indexed over two scans per sample; a large area scan for statistical analysis (240 μm × 360 μm, 500 nm pitch), and a high-resolution scan to more accurately resolve the fine α/α' laths (60 μm × 90 μm, 100 nm pitch). Grain and boundary characteristics were computed from EBSD data using the OIM Analysis V8 software [20], with a grain reconstruction tolerance angle of < 5°. For statistical analyses, a confidence index (CI) filter of > 0.1 was applied to remove the effects of low quality datapoints. Prior-β grain reconstruction was performed according to the Burgers orientation relationship ($\{1\,1\,0\}_\beta \,||\, \{0\,0\,0\,1\}_\alpha$, $\langle 1\bar{1}\,1\rangle_\beta \,||\, \langle 1\,1\bar{2}\,0\rangle_\alpha$) [21,22], with a tolerance angle of < 5° and a minimum probability ratio of 1.1. The morphologies of α/α' laths were described with fitted ellipses, where the minor and major axis diameters were taken as the lath widths and lengths, respectively.

Phase constitution and crystal structure was further investigated by X-ray diffraction (XRD, LabX XRD-6100, Shimadzu) using CuKα radiation (λ = 0.154 nm). XRD profiles were taken on polished *X-Z* planes, with a 1 mm × 10 mm line focus along the entirety of the sample in the *Z* direction. Intensities were collected between the diffraction angles of 30–80° 2θ, at a continuous scan rate of 0.1°.min$^{-1}$ and a pitch of 0.01°. Crystallographic parameters were obtained by the Rietveld refinement method using the open-source Profex/BGMN software [23], starting with reference patterns for α-Ti (COD #9008517) and β-Ti (COD #9008554) from the Crystallography Open Database [24].

Mechanical properties were evaluated by uniaxial tensile testing (AGX50, Shimadzu). Tensile test specimens were extracted from the centre of each test coupon by wire electrical discharge machining with the tensile direction oriented orthogonal to the build direction and parallel to the long edge of the rectangular test coupon (Fig. 1c). This sampling and testing configuration parallel to the build direction was selected for efficiency of powder consumption. In similar microstructures prepared by the same system, the mechanical performance has been reported to be quasi-isotropic [25], thus the sampling is assumed to be valid and representative. The reduced section dimensions of the tensile test specimens were 10 mm × 1 mm × 2 mm. Strain was measured using a non-contact digital video extensometer (TRViewX, Shimadzu) with gauge markers placed at an initial distance of ~8 mm apart to satisfy a gauge length to cross-section proportionality coefficient of $k = 5.65$ (ISO 6892) [26]. Testing was conducted with an initial crosshead speed of 5 × 10$^{-3}$ mm.s$^{-1}$.

**Table 1**
Build parameters used for preparing PBF-LB/M samples. Layer thickness was fixed at 20 μm and laser power was fixed at 160 W.

| Volumetric Energy Density [J.mm$^{-3}$] | 60 | 120 | 180 |
|---|---|---|---|
| Hatch Distance [μm] | Scan Velocity / Linear Energy Density [mm.s$^{-1}$] / [J.mm$^{-1}$] | | |
| 110 (-S) | 1212.1 / 0.13 | 606.1 / 0.26 | 404.0 / 0.40 |
| 150 (-W) | 888.9 / 0.18 | 444.4 / 0.36 | 296.3 / 0.54 |

## 3. Results and discussions

### 3.1. Influence of feedstock characteristics on homogeneity

SEM images of the powders used in this study are presented in Fig. 2. The as-received powders (CP-Ti, 'coarse Fe', 'fine Fe', and pre-alloyed Ti-6Al-4V) are shown in Fig. 2(a–d), while Fig. 2(e,f) show the pre-mixed Ti-1Fe(C) and Ti-1Fe(F) powders (i.e., mixtures of CP-Ti with 'coarse Fe', and 'fine Fe' respectively). The corresponding characteristic diameters ($D_{10}$, $D_{50}$, and $D_{90}$) of the powders are listed along with the evaluated O, N and H content in Table 2.

The CP-Ti and Ti-6Al-4V powders were selected based on their spheroidal morphologies and particle size distributions around ~10–45 μm (i.e., features considered to be favourable for the utilised PBF-LB/M system). Meanwhile, the Fe powders were selected based on availability, and relative size to the CP-Ti powder. In general, finer particles are

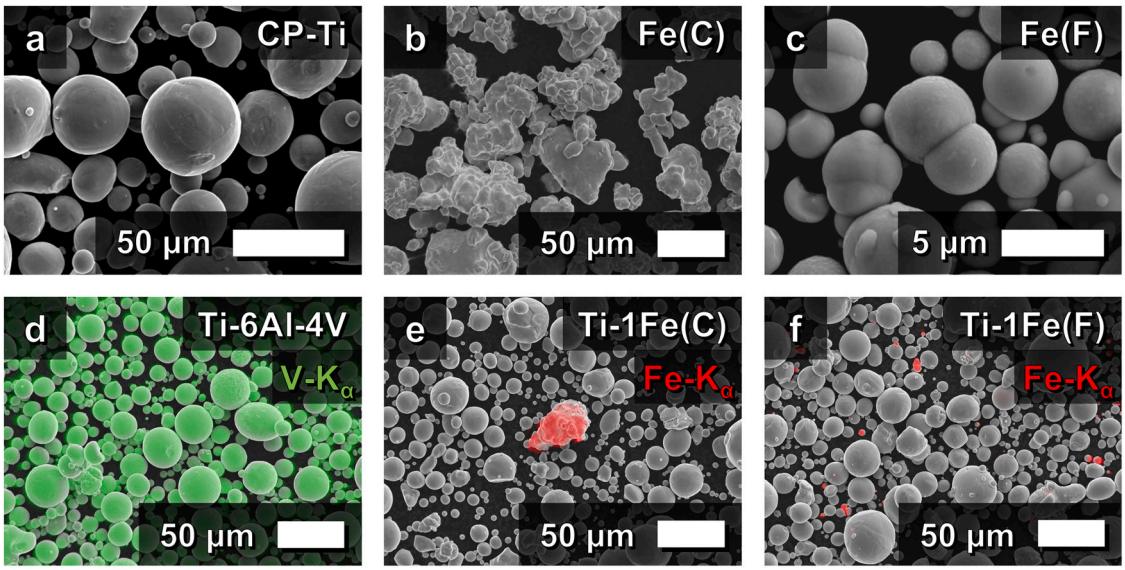


**Fig. 2.** Secondary electron images of all powders used in this study. As-received powders: (a) CP-Ti, (b) coarse Fe, (c) fine Fe, and (d) Ti-6Al-4V. Pre-mixed Ti-1Fe powders: (e) CP-Ti with coarse Fe, and (f) CP-Ti with fine Fe. Characteristic X-ray intensity maps of V-Kα and Fe-Kα are overlayed in colour in (d-f) to highlight the distribution of the primary β-stabilizers in each feedstock.

**Table 2**
Particle size distributions & chemistries of starting powders and mixed feedstocks as evaluated by laser diffraction analysis and inert gas fusion.

| Powder | Characteristic Diameters | | | Chemistry | | | | | |
|---|---|---|---|---|---|---|---|---|---|
| | $D_{10}$ [μm] | $D_{50}$ [μm] | $D_{90}$ [μm] | Ave. O [wt%] | Ave. N [wt%] | Ave. H [wt%] | Ave. Fe [wt%] | Ave. Al [wt%] | Ave. V [wt%] |
| CP-Ti (Gr. 2) | 13.9 | 26.4 | 44.5 | 0.154 ± 0.008 | 0.004 ± 0.0005 | 0.003 ± 0.001 | 0.027* | N.A. | N.A. |
| Coarse Fe (99.9 %) | 24.2 | 40.4 | 65.7 | 0.168 ± 0.005 | 0.005 ± 0.0003 | 0.004 ± 0.001 | Bal. | N.A. | N.A. |
| Fine Fe (99.9 %) | 3.0 | 5.0 | 7.7 | 0.363 ± 0.005 | 0.560 ± 0.014 | 0.005 ± 0.001 | Bal. | N.A. | N.A. |
| Ti−6Al-4V (Gr. 5) | 12.2 | 24.7 | 45.4 | 0.163 ± 0.008 | 0.010 ± 0.001 | 0.007 ± 0.001 | 0.190* | 5.73 | 3.87 |
| Ti−1Fe (C) | 11.6 | 22.7 | 43.2 | 0.145 ± 0.002 | 0.005 ± 0.001 | 0.008 ± 0.001 | 1† | N.A. | N.A. |
| Ti−1Fe (F) | 10.8 | 21.7 | 43.0 | 0.156 ± 0.003 | 0.010 ± 0.0001 | 0.002 ± 0.001 | 1† | N.A. | N.A. |

N.A: Not analysed
* From mill sheet
† Estimated based on powder mixing ratio

considered to be superior for homogenisation when performing in-situ alloying [27]. At the same time, an excess of fine particles also has the potential to result in excessive inter-particle friction in the powder bed, impeding powder flowability and leading to recoating defects in PBF processes [27]. With this consideration, a fine spheroidal Fe powder of ~3–8 μm (approx. one order of magnitude smaller than the CP-Ti powder) was compared with a coarser irregular Fe powder of ~25–65 μm (similar in size to the CP-Ti powder).

Despite this large difference in Fe particle size, the measured particle size distributions of both Ti-1Fe(F) and Ti-1Fe(C) remained close to the initial distribution of the base CP-Ti powder at ~10–45 μm. Considering the small fraction of Fe particles required to attain the target composition of 1 wt% Fe (~0.86 at%), the similarity is reasonable. As a result, both pre-mixed Ti-1Fe feedstocks were observed to exhibit similar flow and spreadability characteristics, independent of Fe particle size and morphology. Qualitatively, both Ti-1Fe feedstocks showed similar building performance to Ti-6Al-4V, with no notable recoating defects during building. This observation suggests powder flowability is not sensitive to Fe particle size in pre-mixed Ti-1Fe feedstocks.

By comparison, a more pronounced difference was the distribution of Fe in the two mixtures. EDS intensity maps of V and Fe characteristic X-rays are overlayed on top of the SEM images in Fig. 2(d–f) to highlight the distribution of the main β-stabilising elements in each of the feedstocks used for PBF-LB/M experiments (Ti-6Al-4V, Ti-1Fe(C) and Ti-1Fe (F)). The pre-alloyed Ti-6Al-4V powder (Fig. 2d) naturally exhibited a homogeneous distribution of V, in clear contrast to the localisation of Fe content in the pre-mixed feedstocks. As expected, the Ti-1Fe(F) mixture (Fig. 2 f) also exhibited superior homogeneity over the Ti-1Fe(C) mixture (Fig. 2e), as the finer particles are free to disperse more evenly amongst the CP-Ti particles. In the two images of comparable area, only a single large Fe particle is observed in Ti-1Fe(C) in contrast to the many fine Fe particles in Ti-1Fe(F).

The effect of feedstock heterogeneity on the in-situ alloying behaviour is highlighted in Fig. 3, which compares the distribution of Fe in microstructures built at 60-S, 120-S, and 180-S. In this comparison, the heterogeneity of the feedstock is seen to be directly inherited in the microstructure of the built materials, with pronounced segregation in the samples built from Ti-1Fe(C) (Fig. 3a), and limited segregation in the samples built from Ti-1Fe(F) (Fig. 3b). In in-situ alloying, the final chemical homogeneity of the part strongly depends on the dilution of solutes in the individual melt pools during building [28]. Under identical laser parameters, the size of the melt pool generated is largely governed by the absorption of laser energy by powder bed, and the efficiency of heat conduction. Both Ti-1Fe(F) and Ti-1Fe(C) consist predominantly of CP-Ti powder, so it is assumed that the two feedstocks share similar laser absorptivity dynamics and therefore similar melt pool geometries under identical build conditions. With this assumption, the more sparse distribution of Fe in Ti-1Fe(C) would directly reduce the likelihood of capture and dissolution in each scan track [29]. As a result, individual melt pools in the processing of Ti-1Fe(C) either fail to capture

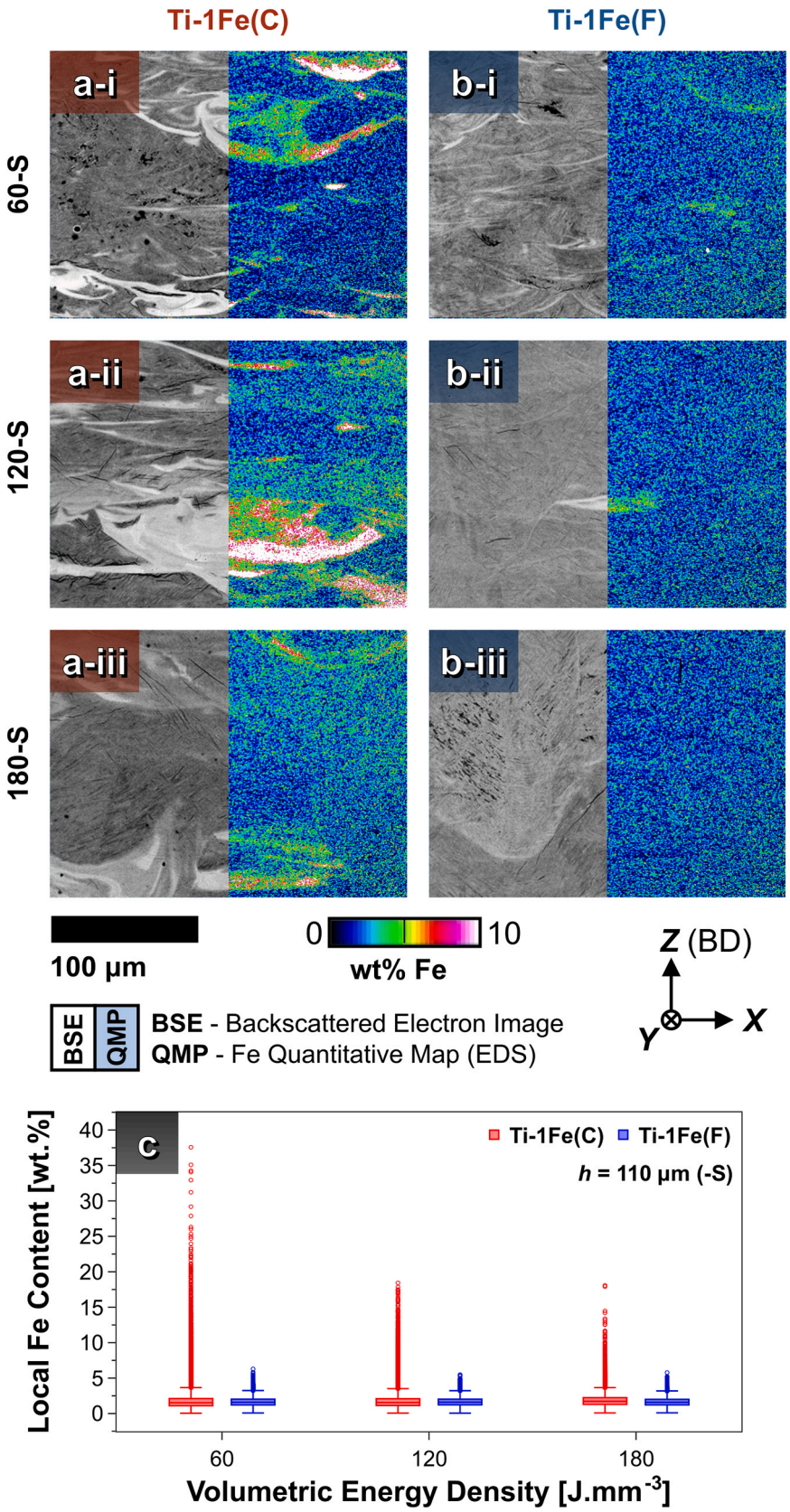


**Fig. 3.** Heterogeneities in the *X-Z* microstructures of Ti-1Fe built from pre-mixed feedstock prepared from (a) coarse Fe and (b) fine Fe powders, as observed by backscattered electron imaging (left half) and Fe EDS quantitative mapping (right half), prepared at (-i) 60-S, (-ii) 120-S, and (-iii) 180-S. (c) Distributions of local Fe concentrations from EDS data from the same samples, evaluated over scanning areas of ~2.4 mm × 1.8 mm.

any significant amount of Fe solutes, or otherwise capture excessive Fe, leading to distinct macro-segregation along scan tracks [30].

When observed in backscattered electron imaging (BSE) mode (where contrast principally reflects local atomic weight) the melt tracks that capture excessive Fe appear as bright, featureless, crescent-shaped bands amongst a matrix of Fe depleted grey and black laths (most distinctly observed in Fig. 3a(i–iii) and Fig. 3b(i)). The swirled appearance of the Fe enriched bands suggests their distribution is governed by Marangoni convection during the molten stage of processing, rather than segregation at the solidification front [31]. Meanwhile, the contrast between grey and black laths indicates the presence of micro-segregation across laths of varying Fe content (with Fe enriched laths appearing grey and high purity laths appearing black). While these microstructural features are also visible in Ti-1Fe(F) (Fig. 3b(i–iii)), they are smaller in scale and more evenly distributed, suggesting an improvement in chemical homogenisation. This improvement is supported by quantitative mapping of the Fe content by EDS, which reveals large micro-segregated regions of $>10$ wt% Fe in Ti-1Fe(C) (Fig. 3a (i–iii)). On the other hand, the limited hotspots in Ti-1Fe(F) only contains around 4 wt% Fe (Fig. 3b(i–ii)). Meanwhile, at 180-S, these Fe enriched regions are almost entirely suppressed (Fig. 3b(iii)).

Fig. 3c shows box-plot distributions of local Fe concentration in samples prepared at 60-S, 120-S and 180-S from coarse and fine Fe powders (as quantified from EDS data obtained over larger ~2.4 mm × 1.8 mm sampling areas on *X-Z* cross sections, shown in Supplementary Figure S1). While all materials show median Fe concentrations close to 1 wt%, the samples prepared from coarse Fe powder show a higher fraction of outlier points with higher Fe content. In the case of coarse powder prepared at 60-S, this includes areas exceeding 35 wt% Fe. In contrast, the samples prepared from fine Fe only show a small number of outliers exceeding ~5 wt% Fe, demonstrating a clear improvement in homogeneity. In spite of this, all samples exhibit some fraction of points exceeding the critical Fe concentration required to fully stabilize the β-Ti phase on quenching (~4 wt% Fe) [10]. Therefore, all samples potentially contain regions of single β phase regions distributed amongst transformed α/α' grains, forming quasi-β-fleck defects in the crescent-shaped enriched Fe regions. These are distinct from classical β-fleck defects, which arise from the partitioning of β-stabilising solutes at the solidification front [32], and are reported to be suppressed by the rapid freezing conditions in PBF-LB/M [33].

Previous studies have indicated that Fe enriched β exhibits a higher hardness than the surrounding α grains in binary Ti-Fe alloys [34]. Therefore, regardless of origin, the widespread and heterogeneous distribution of these solute enriched, hard β regions in Ti-1Fe(C) are expected to be detrimental to mechanical performance due to heterogeneous strain localisation, and metastable ω phases that may exist in the compositional gradients around these enriched areas. Therefore, fine Fe particles are identified to be a key pre-requisite for effective in-situ alloying of Ti-1Fe, to avoid excessive heterogeneity and severe phase and chemical macro-segregation. While such segregation has been controlled for intentionally heterogeneous structures in other material systems [31], only discuss the materials prepared from Ti-1Fe (F) will be discussed henceforth, as the degree of heterogeneity in Ti-1Fe(C) is considered beyond the scope of the present study into the alloy system.

### 3.2. Influence of build parameters on porosity

Building parameters are known to have a significant effect on the microstructure, densification, and defect characteristics of materials prepared by PBF-LB/M [4]. It has become customary practice to discuss these effects in terms of volumetric energy density ($E_V$), a unified parameter which describes the amount of energy input for a given volume of powder bed being processed. For continuous output laser systems, this is described as a function of laser power ($P$), scan velocity ($v$), hatch distance ($h$) and layer thickness ($t$) (Eq. 1). In the present study, pre-mixed Ti-1Fe(F) was built at three different values of $E_V$ (60 J.mm$^{-3}$, 120 J.mm$^{-3}$, and 180 J.mm$^{-3}$), using standard (-S, 110 μm) and wide (-W, 150 μm) $h$ distances to determine optimum parameters for building. To accommodate the particle size distribution, $t$ was fixed at 20 μm, while laser power was arbitrarily fixed at 160 W. The range of investigated parameters were centred around a commercially recommended recipe for processing pre-alloyed Ti-6Al-4V powder with the same PBF-LB/M system, while adjustments to $E_V$ and $h$ were made by tuning $v$ in accordance with Table 1.

$$E_V = \frac{P}{vht} \tag{1}$$

Cross-sectional micrographs of Ti-1Fe(F) are presented in Fig. 4, revealing the quantity and distribution of pores (outlined in red) across the evaluated build parameters. In general, the area fraction of pores increases with both $E_V$ and $h$ (i.e. with reducing $v$). In PBF-LB/M and other molten processes involving a moving heat source, a reduction in $v$ (at a fixed $P$) is understood to cause a transition from conduction melting to keyhole melting [35]. This latter mode produces deep 'keyhole' shaped melt pools as higher process temperatures from an increased linear energy density ($E_L$, Eq. 2) leads to metal vaporisation and gas recoil [36]. In turn, there is an increased likelihood of entrapped gas bubbles on solidification, resulting in the eponymous keyhole pores [37].

$$E_L = \frac{P}{v} \tag{2}$$

In the present dataset, a sharp increase in porosity is observed at an $E_L$ of 0.3 J.mm$^{-1}$ (between the parameters of 120-S and 120-W). This appears to be the critical threshold at which process temperatures exceed the vapor point of the feedstock, promoting the formation of keyhole pores. Beyond this threshold, large spherical pores become prominent, which are spatially aligned along the scan vectors (a well reported characteristics of keyhole pores in PBF-LB/M) [36–38]. This spatial distribution is most clearly observed on the *X-Y* plane of the sample built at 180-W, which exhibited the highest porosity at 0.459 area% (Fig. 4 f). Meanwhile, the 120-S parameter appeared to be most optimal for achieving high density, with a porosity of only 0.07 area% (Fig. 4c).

However, it is important to note that simple area fraction analysis does not adequately account for the smaller crescent-shaped pores observed in the samples built at lower $E_L$. These features appear to be lack-of-fusion (LOF) defects, which are known to arise from the insufficient overlap of adjacent scan tracks due to reduction in melt pool size at low $E_L$ [39]. While these LOF defects constitute a miniscule area fraction (<0.073 %) relative to the larger keyhole pores, these are typically understood to be more detrimental to mechanical properties due to the stress concentrations presented by their sharper, non-spherical boundaries [40]. Indeed, optimum build density is found to be uncorrelated with optimum mechanical properties, as there is a noted trade-off between keyhole pores and homogenisation of the feedstock (discussed in *3.3* and *3.4*)

### 3.3. Influence of build parameters on microstructure

Fig. 5(a–f) shows the α/α' grain structures of Ti-1Fe(F) samples built at the various parameters, as revealed in IPF||Z orientation maps. For comparison, Ti-6Al-4V samples built at 120-S and 180-W are shown in Fig. 5(g–h). Similarly, Fig. 6 shows the retained-β structures under the different conditions, while the various reconstructed prior-β structures are shown in Fig. 7. Meanwhile, the distributions of key morphological parameters and grain boundary characteristics, as derived from EBSD, are compared in Fig. 8.

As seen in Fig. 5, all investigated samples consist primarily of fine hierarchical α/α' laths originating from a martensitic β→α' transformation. This type of microstructure is commonly reported in the case

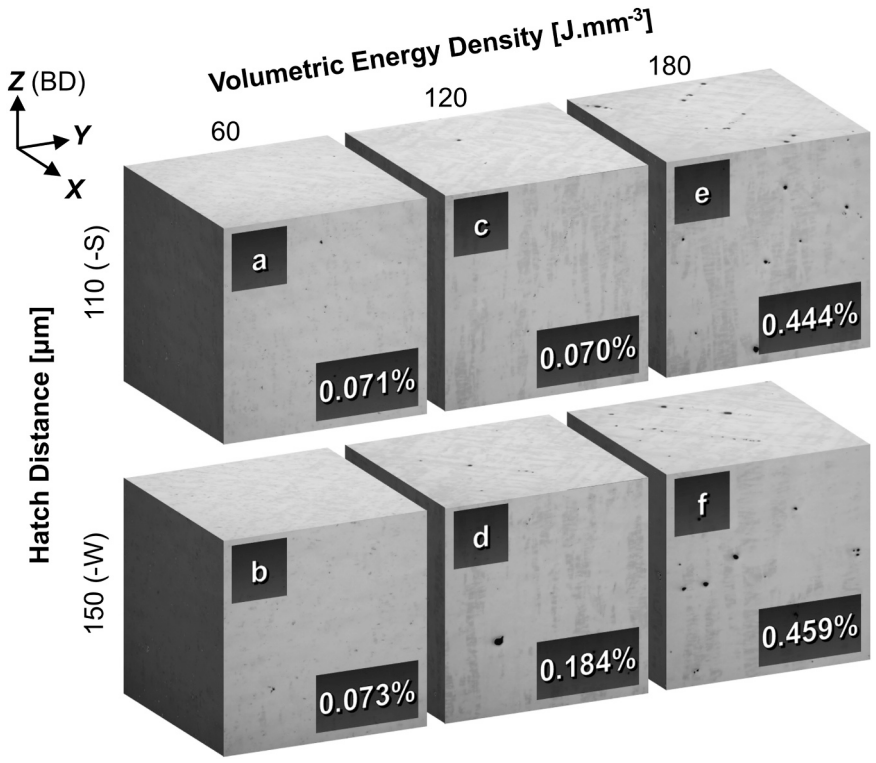


**Fig. 4.** Optical micrographs of *X-Y* and *X-Z* cross sections from Ti-1Fe(F) arranged into representative cubes for each build parameter: (a) 60-S, (b) 60-W, (c) 120-S, (d) 120-W, (e) 180-S, and (f) 180-W. Identified porosity is highlighted with a red border, and each cube is labelled with the areal porosity percentage across both surfaces.

of Ti-6Al-4V, and is understood to be the result of repeated rapid thermal cycling between the β-transus and martensite start temperatures in PBF-LB/M (which impedes diffusion) [41]. Considering the two compositions are close in terms of β-stability [10], this explanation also appears to be valid for PBF-LB/M Ti-1Fe. The grain boundary misorientation distributions (Fig. 8a) are identical across both alloys, revealing a high fraction of α/α inter-variant boundaries across all samples, particularly of the Type 2 ([1 1 −2 0] / 60°) and Type 4 ([−10 5 5 −3] / ~63°) varieties [42]. Indeed, all peaks in all distributions correspond to known boundaries between variants compatible with the Burgers orientation relationship, which evidently suggests that these orientations originate from a martensitic transformation [43].

Looking at the morphology of the reconstructed prior-β structures in Fig. 6(a–f), there is a clear evolution from small, irregular, and more randomly oriented grains at 60-S, 60-W, and 120-S (Fig. 6(a–c)) towards large, columnar prior-β grains with a strong $< 001 >_{\beta} \,||\, Z$ preferred orientation at 120-W, 180-S, and 180-W (Fig. 6(d–f)). Naturally, this shift is accompanied by a sharp rise the maximum texture $\{001\}_{\beta}$ from 6.79 multiples of uniform distribution (MUD) at 60-S, to 29.6 MUD at 180-W. This relationship between texture and build parameter is also seen in the retained β and transformed α/α' grains of the final microstructure, although at lower maximum intensities (Fig. 7). The retained $\{001\}_{\beta}$ grain textures increase from a maximum of 2.88 MUD at 60-S to a maximum of 7.85 MUD at 180-W, while the transformed $\{0001\}_{\alpha}$ textures increase from a minimum of 5.49 MUD at 60-S and 60-W, to a maximum of 10.3 MUD in 120-W, before reducing slightly again to ~8 MUD. It is reasonable to expect some degree of texture inheritance from the prior-β grain structure, given the orientations of the transformed α/α' grains are constrained by the Burgers orientation relationship. The weakening of texture may be explained by the increased number of possible variants (up to 12) within a single prior-β grain [21,42].

This evolution in prior-β morphology towards columnar grains at higher $E_L$ is understood to be an inherent result of the widely reported columnar-to-equiaxed transition [44]. For a given composition, an increased solidification rate suppresses the growth rate of grains, promoting heterogeneous nucleation and competing growth of equiaxed prior-β grains. Conversely, slower solidification rates promote epitaxial growth leading to the formation of large columnar prior-β grains. This transition has been observed in other Ti alloys, including Ti-6Al-4V [45–47]. However, both Ti-6Al-4V samples in the present study show little sensitivity to build parameters, with no notable changes to texture intensity, prior-β column widths, or α/α' lath dimensions. This observation seems to imply that the parametric threshold for this transition is lower for Ti-6Al-4V compared to Ti-1Fe(F); i.e., the critical $E_L$ value required to form columnar prior-β grains in Ti-1Fe(F) is higher than that of Ti-6Al-4V. This is clearly seen at the parameter of 120-S, where Ti-1Fe (F) (Fig. 6c) exhibits a finer grain structure with lower texture than Ti-6Al-4V (Fig. 6g). Two contributions may account for this difference: (i) the Ti-1Fe composition presenting a higher growth restriction factor ($Q$), and (ii) regions of Fe segregation interrupting epitaxial growth. Fe is known to have a $Q$ value in Ti, which favours equiaxed solidification. Simonelli et al. exploited this mechanism to induce progressive refinement of prior-β grains in PBF-LB/M Ti-6Al-4V with Fe addition up to 3 wt% [48]. On top of this effect, the reduced mixing of the pre-mixed feedstocks at lower $E_L$ is seen to produce some quasi-β-fleck defects arranged along melt pool boundaries (as discussed in *3.1* and indicated by dashed white lines in Fig. 6 and Fig. 7). These regions of Fe enrichment, distributed perpendicular to the build direction, also potentially impede epitaxial growth by altering the local solidification conditions. These defects are evidently suppressed at higher $E_L$, with a reduction in retained β fraction from a maximum of 11 area% in 120-S to a minimum of 2.2 area% at 180-S.

Nevertheless, at higher $E_L$, both Ti-6Al-4V and Ti-1Fe(F) solidify in the columnar solidification regime, producing microstructures that are indistinguishable in terms of grain size, texture, and morphology (Fig. 5 (e-h), Fig. 6(e-h)). The differences between these microstructures are only discernible in the XRD profiles (Fig. 9). Specifically, the α/α' peaks of Ti-1Fe are positioned to the left of Ti-6Al-4V, much closer to the

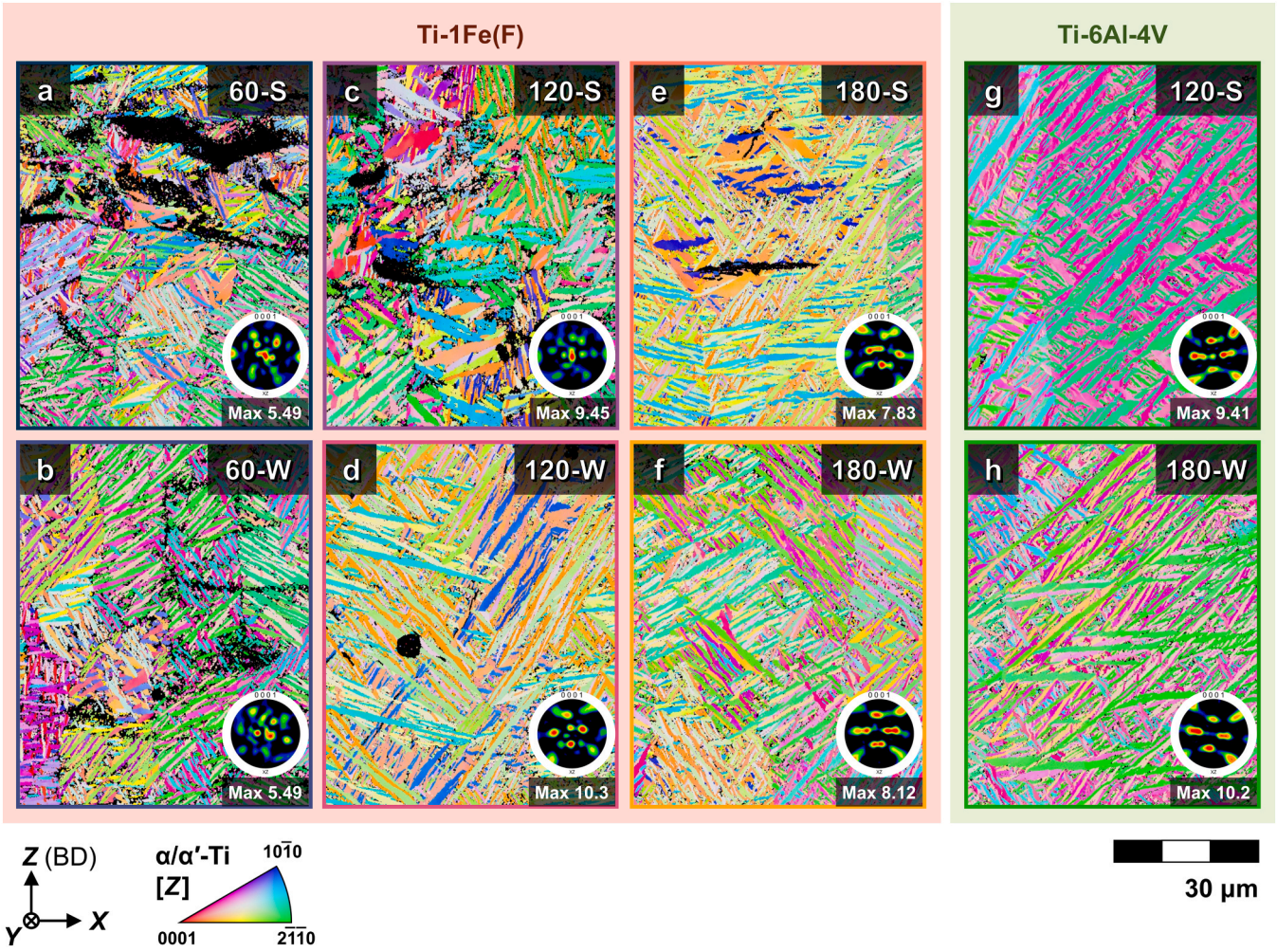


**Fig. 5.** Inverse pole figure (IPF) ∥ *Z* maps of α/α′-Ti grains indexed on *X-Z* cross sections of Ti-1Fe(F) built at (a) 60-S, (b) 120-S, (c) 180-S, (d) 60-W, (e) 120-W, and (f) 180-W; and Ti-6Al-4V built at (g) 120-S, and (h) 180-W. Electron diffraction data was collected with a step size of 0.1 μm. Inset orientation distributions of {0001} poles, and maximum crystallographic texture in units of MUD (multiples of unity distribution) were calculated from wider area scans (240 μm × 360 μm) taken with a step size of 0.5 μm. Black regions represent points not indexed to α/α′-Ti with a confidence index of at least 0.1.

expected positions of α-Ti, indicating a less distorted HCP lattice. Meanwhile, the trace $\{200\}_\beta$ peak of Ti-1Fe appears to be positioned to the right of Ti-6Al-4V, suggesting a slight compression of the BCC lattice relative to Ti-6Al-4V (although this is not conclusive due to the low signal-to-noise of this low-intensity peak) (Fig. 9c). These observed peak shifts are consistent with the different substitutional solute contents between the two compositions, with the higher Al and V content expected to produce a greater magnitude of distortion from an ideal α-Ti lattice. Compared to the ideal α-Ti lattice parameters of $a = 0.2950$ nm and $c = 0.4686$ ($c/a = 1.588$), Rietveld analysis of the Ti-1Fe(F) profiles suggest a slight expansion of both the *a*-axis (0.2959 nm) and *c*-axis (0.4692 nm) ($c/a = 1.586$). Meanwhile, the Ti-6Al-4V profiles presented a more significant contraction of both the *a*-axis (0.293 nm) and *c*-axis = 0.467 nm ($c/a$ =1.593). Small fluctuations in refined lattice parameters were observed across different build parameters (Fig. 9d), likely arising from a partitioning of solutes to β under different states of homogenisation. Despite the observed heterogeneity at lower $E_L$, no elemental Fe peaks were detected in any of the XRD profiles, indicating a complete dissolution of Fe into the Ti matrix.

### 3.4. Mechanical properties

Representative engineering stress-strain curves for all evaluated samples are compared in Fig. 10a, while the averages and standard deviations for 0.2 % yield strength ($\sigma_{YS}$), ultimate tensile strength ($\sigma_{UTS}$), and strain at fracture ($\varepsilon_F$) are summarised in Table 3. Representative curves, averages and standard deviations of each property are obtained from the results of three tensile specimens, extracted from the centre of each coupon (Fig. 1b,c) and subjected to uniaxial tension in the *Y* direction. In alignment with microstructure trends, the tensile properties of samples built from pre-alloyed Ti-6Al-4V were found to be largely insensitive to build-parameters, while the pre-mixed Ti-1Fe(F) samples showed a clear sensitivity to $E_L$. The sample prepared at 60-S (lowest $E_L$ condition, 0.09 J.mm$^{-1}$) exhibited the highest strength ($\sigma_{YS}$ = 1027.8 ± 25.0 MPa, $\sigma_{UTS}$ = 1161.5 ± 25.5 MPa), but the lowest ductility ($\varepsilon_F$ = 3.8 ± 1.2 %). As $E_L$ was increased through the investigated parameters, ductility gradually improved at the cost of strength, with 180-W (highest $E_L$ condition, 0.54 J.mm$^{-1}$) exhibiting the best ductility ($\varepsilon_F$ = 12.2 ± 1.1 %) and lowest strength ($\sigma_{YS}$ = 942.8 ± 33.8 MPa, $\sigma_{UTS}$ = 1030.1 ± 27.2 MPa). In general, the wider *h* (150 μm) also improved ductility at the cost of $\sigma_{UTS}$. The reduced ductility at lower $E_L$ is likely related to the presence of both embrittling retained β (as discussed in *3.1*, *3.3*), and LOF defects (as discussed in *3.2*).

The properties of Ti-1Fe(F) prepared at 120-W and 180-W also appeared to be consistent with the results recently reported by Liu et al. [17]. Their study also utilised an in-situ alloying route; however, they attained these properties at much lower energy densities ($E_V$ = 60 J.

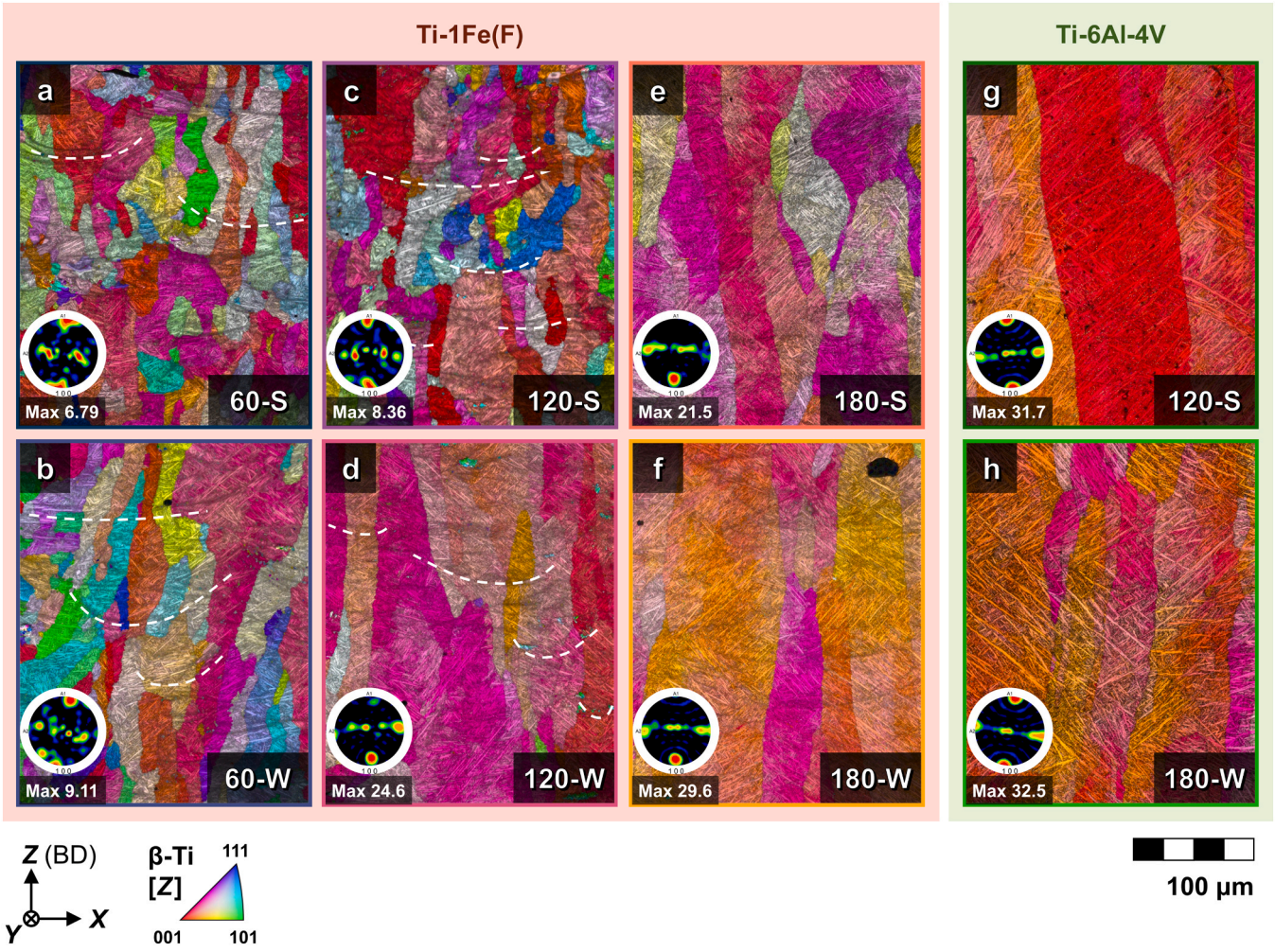


**Fig. 6.** IPF ‖ *Z* maps of reconstructed parent (bottom-left) β-Ti grains indexed on *X-Z* cross sections of Ti-1Fe(F) built at (a) 60-S, (b) 60-W, (c) 120-S, (d) 120-W, (e) 180-S, and (f) 180-W; and Ti-6Al-4V built at (g) 120-S, and (h) 180-W. Electron diffraction data was collected with a step size of 0.1 μm. Inset are orientation distributions of $\{001\}_\beta$ poles, maximum crystallographic texture in units of MUD (multiples of unity distribution). Black regions represent points not indexed to β-Ti with a confidence index of at least 0.1.

$mm^{-3}$, $E_L = 0.18$ $J.mm^{-1}$). This discrepancy likely arises from their use of finer Fe particles (~0.3 μm), higher laser power (180 W), and a larger beam diameter (64 μm), which are all conducive to improving the homogenisation of Fe (via increased Fe dispersion and larger melt pools) [29,30]. In combination with their datasets, our results affirm the importance of homogeneity in realising good ductility in Ti-1Fe prepared by PBF-LB/M. As long as this pre-requisite is met, the overall performance of as-built Ti-1Fe are excellent, exceeding both the strength ($\sigma_{YS} \geq 820$ MPa, $\sigma_{UTS} \geq 895$ MPa) and ductility ($\varepsilon_f \geq 10$ %) requirements for additively manufactured Ti-6Al-4V (as outlined ASTM F2924) [7]. Indeed, all samples exhibited properties within the range those reported in literature for PBF-LB/M Ti-6Al-4V (Fig. 10c) [6,49–58], as well as significant strengthening over PBF-LB/M CP-Ti [25,59–63], despite the relatively lean solute content of Ti-1Fe; demonstrating the viability of Ti-1Fe as a substitute for Ti-6Al-4V in terms of quasi-static tensile performance.

Compared with Ti-1Fe(F), the Ti-6Al-4V samples built from pre-alloyed powder are still about 100–200 MPa stronger ($\sigma_{YS} \approx 1130$ MPa, $\sigma_{UTS} \approx 1235$ MPa). However, in parts designed around these standards for room temperature applications, there is limited benefit to an extra 100–200 MPa of strength apart from an additional factor of safety. In terms of toughness, the loss in strength is adequately compensated for, by the slight increase in ductility under optimal processing conditions. A comparison of the toughness moduli (obtained from the integrated areas under the tensile curves) reveals an identical toughness of ~119 $MJ.m^{-3}$ at the 180-W build parameter. Furthermore, this gap in strength between Ti-1Fe and Ti-6Al-4V is also much lower in PBF-LB/M than in other conventional processes (Fig. 10c). In literature, Ti-1Fe-0.3O-0.04 N is reported to have as-cast properties of $\sigma_{YS} = 603$ MPa and $\sigma_{UTS} = 645$ MPa, which is about 300 MPa less than similarly prepared Ti-6Al-4V [11]. Meanwhile, wrought (extruded, equiaxed) Ti-1Fe microstructures are reported with $\sigma_{YS} = 651.3$ MPa and $\sigma_{UTS} = 762.1$ MPa [34], though this still falls short of the ASTM standards for wrought Ti-6Al-4V [64]. Amongst conventional processes, the properties of Ti-6Al-4V are only reproducible in Ti-1Fe via water-quenched martensitic microstructures ($\sigma_{UTS} = 900$ MPa) [16]. However, in practice, this approach is limited to smaller parts with uniform cross sections due to the sensitivity to cooling rates. In contrast to these conventionally processed materials, PBF-LB/M appears to be uniquely advantageous for obtaining high strengths from Ti-1Fe with fewer geometric restrictions.

The similarity between Ti-1Fe and Ti-6Al-4V extends to flow behaviour, as seen in the work hardening curves presented in Fig. 10b. All curves show continuous yielding behaviour, with an observed trade-off between hardening rate and uniform elongation. Ti-1Fe(F) built at 60-S and 60-W exhibited the highest initial work hardening, but only exhibited 3.7 % and 3.8 % uniform elongation, respectively. The microstructures of these samples were characterised by a high fraction of

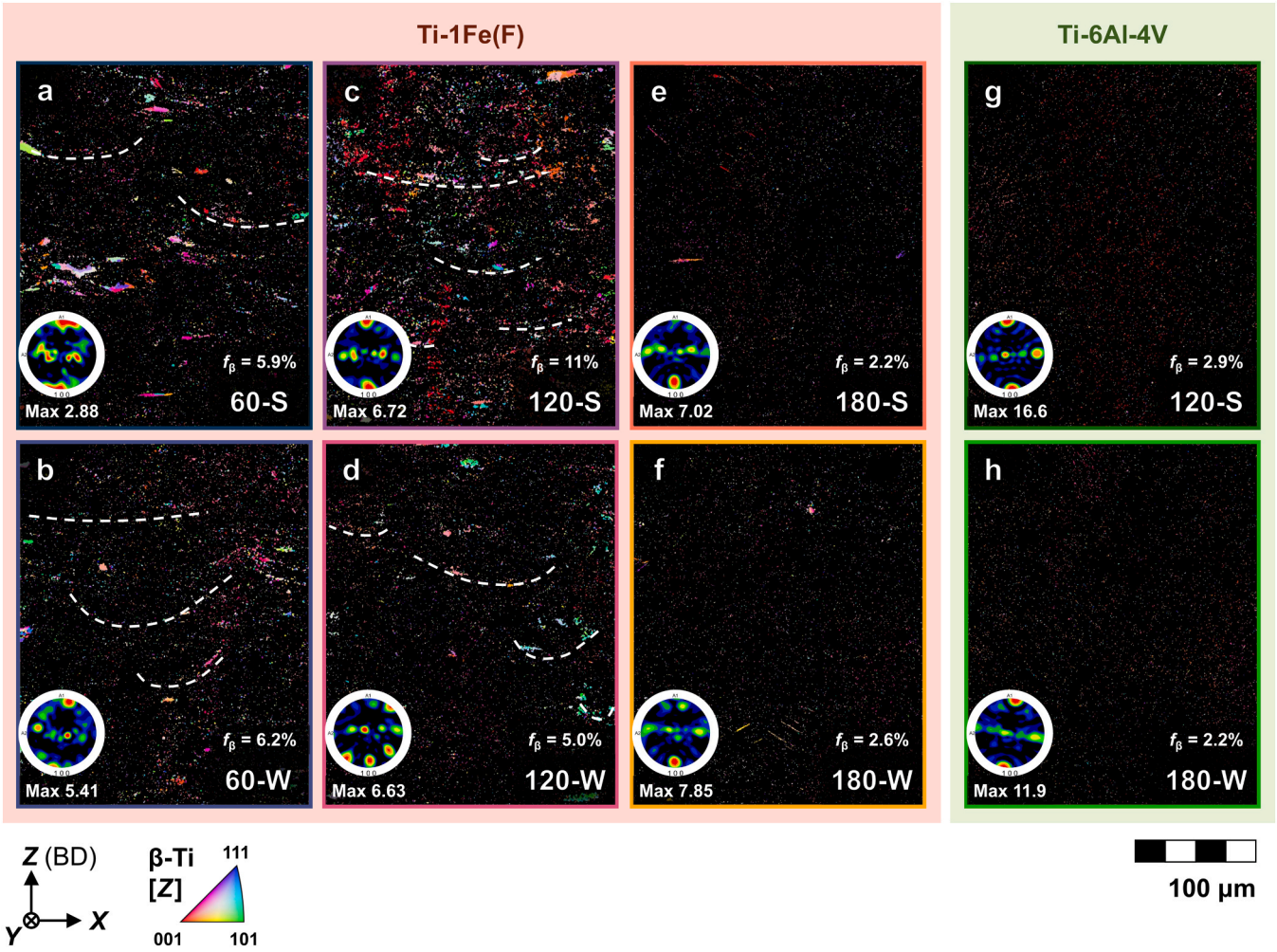


**Fig. 7.** IPF ‖ *Z* maps of β-Ti grains indexed on *X-Z* cross sections of Ti-1Fe(F) built at (a) 60-S, (b) 60-W, (c) 120-S, (d) 120-W, (e) 180-S, and (f) 180-W; and Ti-6Al-4V built at (g) 120-S, and (h) 180-W. Electron diffraction data was collected with a step size of 0.1 μm. Inset are orientation distributions of $\{001\}_\beta$ poles, maximum crystallographic texture in units of MUD (multiples of unity distribution), and retained beta fraction. Black regions represent points not indexed to β-Ti with a confidence index of at least 0.1.

LOF defects, refined prior β grains, and shorter α/α' laths of more varied orientations. These features are all promoters of strain localisation. The Ti-6Al-4V samples initially follow a similar hardening curve to these samples, before flattening out more abruptly to support a uniform elongation of 4.4 %. The rest of the Ti-1Fe(F) samples exhibit lower initial hardening but incrementally delayed the onset of necking up from 4.5 % (120-S) to 5.2 % (180-W). Notably, all samples prepared using the wider *h* (150 μm) exhibited superior uniform elongation at the expense of work hardening. This likely arises from process related O and N pickup, leading to differences in interstitial content (discussed in section 3.5).

Fracture surfaces of the Ti-1Fe(F) samples built at the various conditions are shown in Fig. 11. All samples exhibit a mix of fine dimples on larger faceted surfaces with sizes correlated to prior-β grain size. This aligns well with the reported 'terraced' fracture behaviour of PBF-LB/M Ti-6Al-4V, where the fine dimples correspond to local plastic deformation of α/α' grains, and the facets correspond to intergranular crack paths which propagate along similarly oriented α/α' clusters originating from single prior-β grains [52,58]. This is most evident at higher $E_L$ (Fig. 11(e,f)), where the facets clearly reveal columnar prior-β structures. Meanwhile, LOF defects are clearly observed on the fracture surfaces of the Ti-1Fe(F) samples prepared at lower $E_L$ (Fig. 11(a,b)), confirming that they are indeed a significant embrittling factor.

### 3.5. Strengthening mechanisms and elemental contributions

Based on the chemical compositions and observed microstructures, three strengthening mechanisms were identified as likely contributors to the high yield strengths of the Ti-1Fe alloys, namely solid solution strengthening, grain boundary strengthening, and dislocation strengthening. To quantify the theoretical contributions of each mechanism, a combination strengthening model (Eq. 3) was used to predict yield strength ($\sigma_{YS}$) from the observed microstructures.

$$\sigma_{YS} = \sigma_0 + \Delta\sigma_{SS} + \Delta\sigma_{GB} + \Delta\sigma_{DS} \quad (3)$$

In this model, $\sigma_{YS}$ is estimated as the simple sum of the intrinsic lattice friction ($\sigma_0$) and contributions from solid solution strengthening ($\Delta\sigma_{SS}$), grain boundary strengthening ($\Delta\sigma_{GR}$), dislocation strengthening ($\Delta\sigma_{DS}$). Because all samples were predominantly α-Ti, only this phase was considered for modelling. In α-Ti, the prismatic slip system is reported to be the most readily activated at room temperature. Accordingly, the critical resolved shear stress of this slip system (~ 90 MPa) was taken as $\sigma_0$ [66].

Solid solution strengthening occurs when dislocation movement is impeded by impurity solute atoms in a lattice. This mechanism is typically described by the Labusch model, which relates the strengthening contribution in a binary system to the solute concentration with a two-thirds-power dependence [67]. In multi-component systems, the

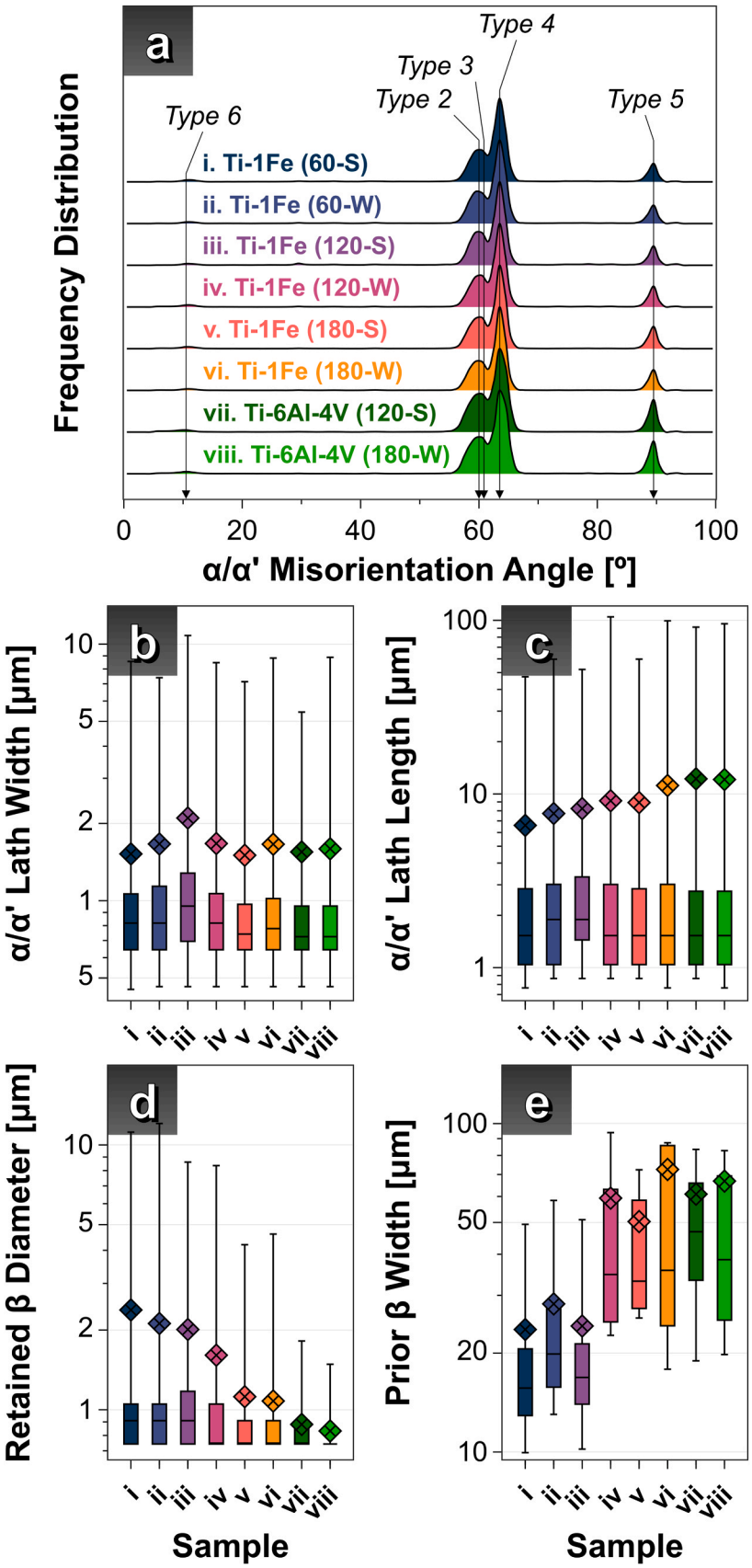


**Fig. 8.** (a) Distributions of correlated misorientation angles at reconstructed α/α' boundaries. Box plots showing distributions of (b) α/α' lath widths, (c) α/α' lath lengths, (d) retained β diameters, and (e) reconstructed prior-β widths. Area averages are indicated by the diamond marker. (i-viii) refer to Ti-1Fe(S) built at (i) 60-S, (ii) 60-W, (iii) 120-S, (iv) 120-W, (v) 180-S, (vi) 180-W, and Ti-6Al-4V built at (vii) 120-S and (viii) 120-W.

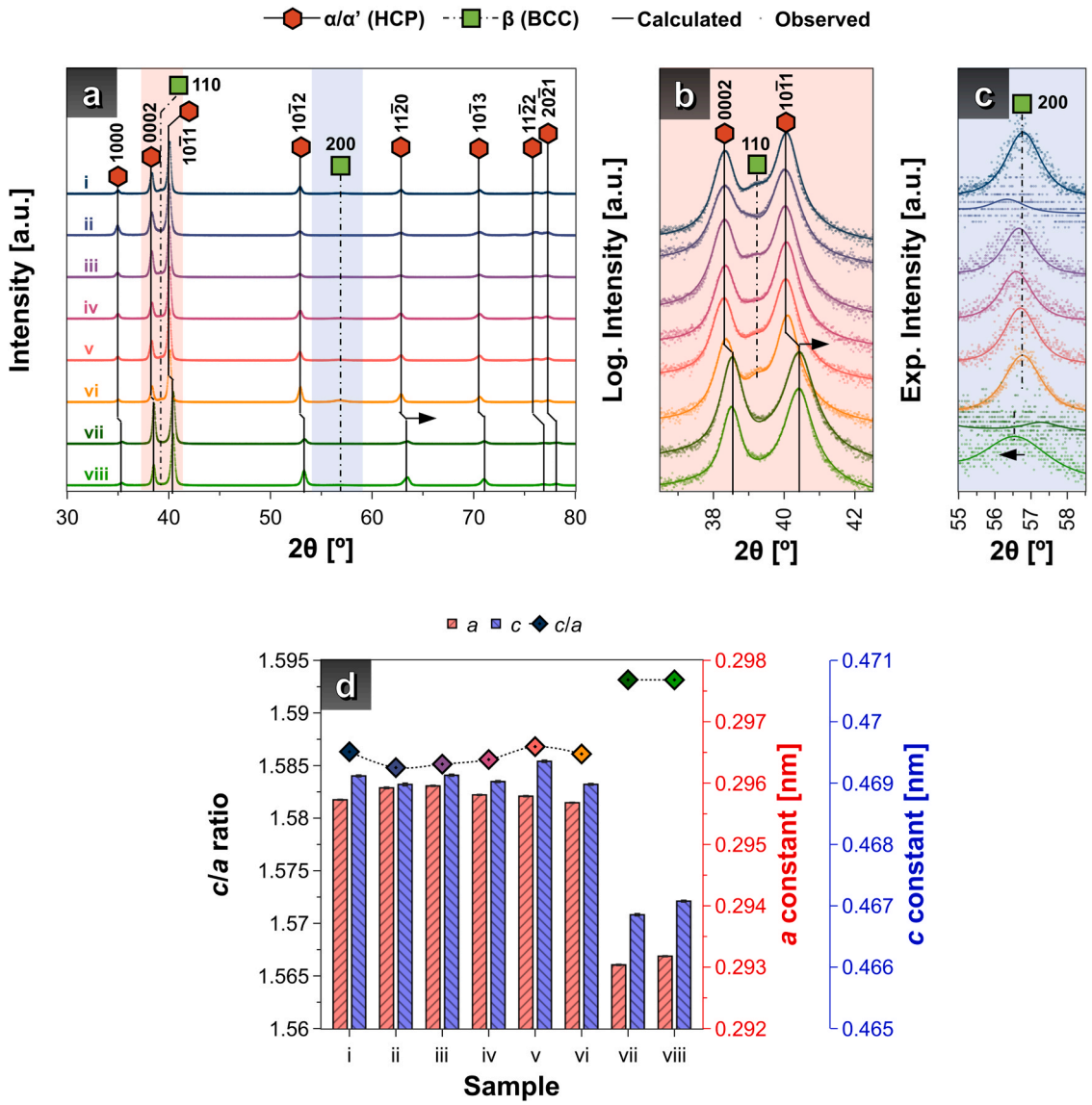


**Fig. 9.** (a) X-ray diffraction patterns of Ti-1Fe(S) built at (i) 60-S, (ii) 60-W, (iii) 120-S, (iv) 120-W, (v) 180-S, (vi) 180-W, and Ti-6Al-4V built at (vii) 120-S and (viii) 120-W. (b) Detail view of the $(0002)_\alpha$, $(110)_\beta$ and $(10\bar{1}1)_\alpha$ peaks with logarithmic intensity scale. (c) Detail view of the $(200)_\beta$ peak with exponential intensity scale. Observed intensities are plotted as points and calculated profiles are plotted as lines.

contributions of each individual element can be compounded by Eq. 4, where $x_i$ is the concentration of any solute $i$, and $B_i$ is the strengthening constant of solute $i$ in the solvent phase [68,69].

$$\Delta\sigma_{SS} = \left(\sum_i B_i^{\frac{3}{2}} x_i\right)^{\frac{2}{3}} \tag{4}$$

Galindo-Fernandez et al. proposed a generalised model to predict the strength of Ti-6Al-4V of various microstructures, including those prepared by PBF-LB/M [70]. In their work, they report theoretically calculated values of $B_{Al}$ and $B_V$ in α-Ti as 1813 MPa.at$^{2/3}$ and 127 MPa.at$^{2/3}$, respectively. These values are adapted for calculating predicted strengths for the present Ti-6Al-4V samples. Although the significance of interstitial O and N strengthening in Ti is well established [71], it is not possible to theoretically calculate $B_O$ and $B_N$ as there is no appropriate method to compare the shear modulus mismatch of these elements. Therefore, experimentally fitted values for $B_O$ (9068 MPa.at$^{2/3}$) and $B_N$ (9284 MPa.at$^{2/3}$) have been adapted from our previous works to determine the strengthening contributions from O and N [72]. In these works, the strengthening coefficients are reported as $B_i/S_F$ values. For the present model, these are converted to $B_i$ values using $S_F = 0.37$, in alignment with the microstructures initially used to obtain these values [59,60]. By a similar method, a value for $B_{Fe}$ (1985 MPa.at$^{2/3}$) was adapted from [73].

Grain boundary strengthening arises from the impedance of dislocation transfer across high angle crystallographic boundaries. As grains are refined, a higher applied stress is required to activate dislocation transfer, as described by the Hall-Petch relationship (Eq. 5). This well-known equation relates the increase in yield strength from grain boundary strengthening to a factor ($k_Y$) and the average grain diameter ($d$). In the present PBF-LB/M microstructures, the laths exhibit high aspect ratios, and do not form similarly oriented colonies. This implies that effective slip length is constrained to individual laths [52]. Accordingly, average lath widths estimated by elliptical fitting of EBSD data have been used for calculation instead of equivalent spherical grain diameters. Meanwhile, a coefficient $k_Y$ of 300 MPa.μm$^{-1/2}$ was adapted from Galindo-Fernandez [70].

$$\Delta\sigma_{GB} = k_Y d^{-\frac{1}{2}} \tag{5}$$

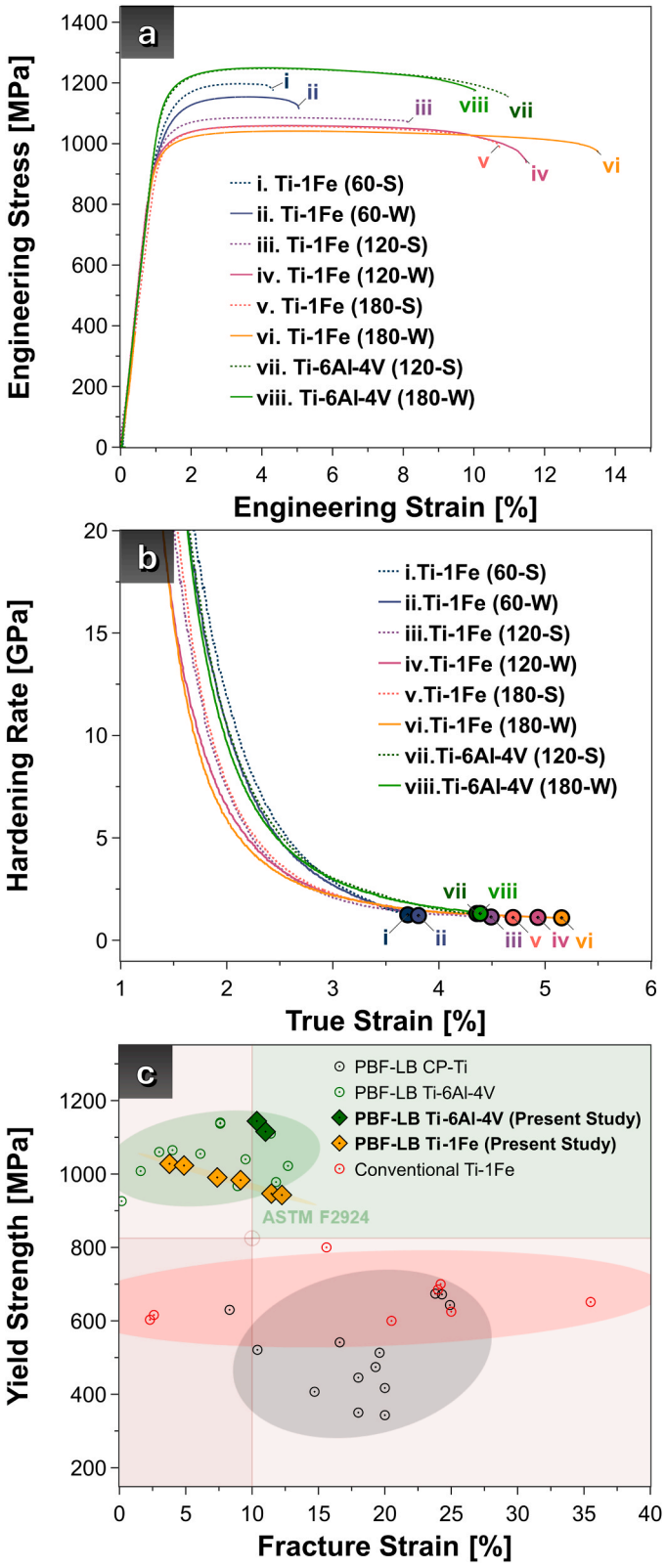


**Fig. 10.** (a) Engineering stress-strain and (b) work-hardening curves (up to necking) obtained from uniaxial tensile testing perpendicular to the build direction. (c) Comparison of yield strengths and fracture strains of the samples prepared in the present study (solid diamonds), and reported properties of PBF-LB/M CP-Ti (Grades 1–4) [25,59–63], PBF-LB/M Ti-6Al-4V [6,49–58], and conventionally prepared Ti-1Fe [11,16,34,65] from literature (open circles). The minimum requirements for AM Ti-6Al-4V (ASTM F2924) are marked by the solid lines [7].

As-built PBF specimens are known to contain a high density of dislocations retained from the martensitic transformation [74]. Therefore, dislocation strengthening is factored into the present model via the Taylor relationship (Eq. 6). This equation relates the increase in yield strength with the Taylor factor ($M$), shear modulus ($G$), dislocation density ($\rho$), and an interaction factor $\alpha$ (~0.2 for Ti [75]). According to Ashby's hardening model, initial stages of work hardening (i.e. the onset of yielding) are predominantly governed by geometrically necessary dislocations (GNDs). Accordingly, average GND densities calculated from local misorientations in the EBSD data have been used for calculations [76]. Similarly, the average Taylor factor derived from EBSD data was used in the present model.

$$\sigma_{DS} = MGb\alpha\rho^{\frac{1}{2}} \tag{6}$$

The calculated strengthening contributions are presented in Fig. 12a, along with the experimentally observed $\sigma_{YS}$ values. Meanwhile, the corresponding model parameters and experimentally derived sample variables are listed in Table 4 and Table 5, respectively. For clarity, the calculated contribution from each variable is presented in parentheses in Table 5.

Evidently, this theoretical framework provides an excellent description for the experimental $\sigma_{YS}$ values of the Ti-6Al-4V samples, and the Ti-1Fe(F) samples built at higher $E_L$ values. In contrast, the $\sigma_{YS}$ values of the Ti-1Fe(F) samples built at lower $E_L$ appears to be generally underpredicted. This discrepancy is likely attributable to an increased fraction of retained β-phase in these samples, which are not accounted for by the model. These retained β regions, which introduce additional phase boundaries and exhibit significant local Fe enrichment, are expected to contribute an additional strengthening effect beyond those currently modelled. However, given the associated reduction in ductility and the marginal relevance of these microstructures to the intended design criteria, further analysis of this effect was not pursued.

More importantly, the close alignment between experimental and observed $\sigma_{YS}$ values in the high-performing Ti-1Fe(F) samples highlights grain boundary strengthening, dislocation strengthening, and O/N solid solution strengthening as the dominant mechanisms in defect-free conditions. In the case of Ti-6Al-4V, an additional contribution arises from Al solid solution strengthening, estimated at approximately 300 MPa. Notably, the Ti-1Fe(F) alloys appear to feature slightly elevated N content (particularly in the 180-S condition, where it nearly doubles that of Ti-6Al-4V) which appears to partially offset the loss in strength from the absence of Al. This observation suggests that these high-performing samples may be more appropriately regarded as Ti-1Fe-0.1 N alloys, given that their N concentrations exceed those typically found in both Ti-6Al-4V and CP-Ti.

Considering this discrepancy, it becomes important to understand the kinetics of this elevation in interstitial content. The O, N and H contents of the as-built samples, as evaluated by inert gas fusion (IGF) are shown in Fig. 12b, revealing a considerable amount of process related pickup of the interstitial elements. Despite the use of an argon processing atmosphere, the interstitial content in Ti-1Fe(F) rises considerably by at least + 0.024 wt% O and + 0.04 wt% N after building (from 0.156 % O and 0.009 wt% N in the feedstock to 0.180 wt% O and 0.049 wt% N in the samples built at 60-W). The mechanism of this pickup from process effects such as spatter and adsorption is well described in literature [77,78]. O and N pickup intensifies with further increases to $E_V$ and decreases to $h$, likely in relation to intensified melt pool activity [78]. At 180-S, the highest interstitial content is observed at 0.238 wt% O and 0.124 wt% N. Similarly, the interstitial content in the built Ti-6Al-4V samples is elevated by about + 0.079 wt% O and + 0.062 wt% N over its feedstock (to ~0.25 wt% O and ~0.07 wt% N). The higher N content in the finer Fe powders (Table 2) is also considered to be a major source of introduction into the material. Meanwhile, all samples show a similar H content of ~0.008 wt% with no clear relation to build parameter. Comparing these values, Ti-1Fe(F) appears to

**Table 3**
Averages and standard deviations of evaluated tensile properties.

| Sample | 0.2 % Yield Strength [MPa] | | Tensile Strength [MPa] | | Fracture Strain [%] | | Toughness Modulus [MJ.m$^{-3}$] | |
|---|---|---|---|---|---|---|---|---|
| | Ave. | Std. Dev. | Ave. | Std. Dev. | Ave. | Std. Dev. | Ave. | Std. Dev. |
| Ti−1Fe(F) (060-S) | 1027.8 | 25.0 | 1161.5 | 25.5 | 3.8 | 1.2 | 36.3 | 13.4 |
| Ti−1Fe(F) (060-W) | 1023.1 | 8.6 | 1164.2 | 8.2 | 4.9 | 0.9 | 48.6 | 10.1 |
| Ti−1Fe(F) (120-S) | 990.6 | 27.7 | 1087.1 | 22.8 | 7.4 | 0.6 | 73.6 | 6.5 |
| Ti−1Fe(F) (120-W) | 946.6 | 28.6 | 1045.1 | 24.2 | 11.5 | 1.5 | 112.1 | 13.1 |
| Ti−1Fe(F) (180-S) | 983.4 | 37.1 | 1061.0 | 28.6 | 9.1 | 1.2 | 90.0 | 12.5 |
| Ti−1Fe(F) (180-W) | 942.8 | 33.8 | 1030.1 | 27.2 | 12.2 | 1.1 | 118.6 | 11.3 |
| Ti−6Al-4V (120-S) | 1115.4 | 17.6 | 1229.0 | 15.9 | 11.0 | 0.9 | 125.7 | 11.3 |
| Ti−6Al-4V (180-W) | 1144.0 | 9.5 | 1240.0 | 10.4 | 10.4 | 0.8 | 118.9 | 10.6 |

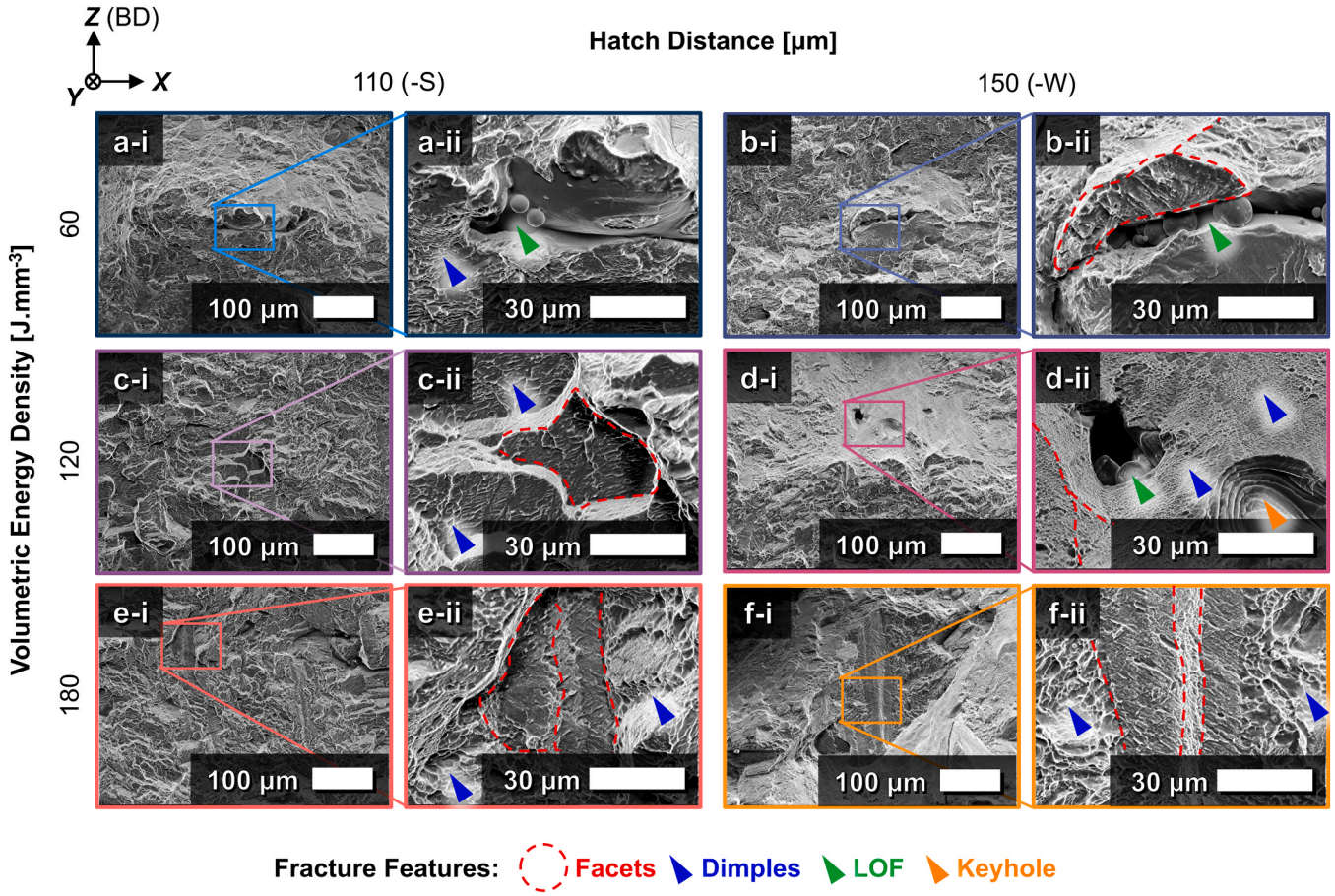


**Fig. 11.** Typical fracture surfaces of Ti-1Fe(F) built at (a) 60-S, (b) 120-S, (c) 180-S, (d) 60-W, (e) 120-W, and (f) 180-W; and Ti-6Al-4V built at (g) 120-S, and (h) 180-W, at (-i) low and (-ii) high magnifications. Fracture surface features are annotated by dashed lines and arrows.

exhibit a higher sensitivity to N pickup, while Ti-6Al-4V showed greater to O pickup.

Remarkably, the elevated levels of interstitial pickup observed in our samples do not appear to significantly impair ductility, despite exceeding the limits prescribed by ASTM standards for unalloyed titanium [79] and Ti-6Al-4V [64]. Our previous studies have shown that the rapid solidification inherent to additive manufacturing (AM) processes can suppress the segregation of interstitial elements such as O and N, thereby mitigating their embrittling effects [60,72]. Additionally, the combined sensitivity to O/N has been reported to diminish with grain refinement [59,80]. Given the refined microstructures and rapid solidification characteristic of our PBF-LB/M-processed materials, it is reasonable to infer that these mechanisms are operative in the present samples.

In contrast to the interstitial solutes, ICP-OES analysis reveals the Fe concentration to be mostly stable with an average of 1.035 ± 0.054 wt% Fe across the various build parameters. Moreover, in contrast to prior reports [81], the small variation in Fe content did not exhibit any clear correlation to either $E_L$ or $E_V$. Together, suggests elemental loss through preferential evaporation of Fe was not a significant factor in our system. By Eq. 4, this range of Fe concentration corresponds to an average strengthening contribution of 38.3 ± 3.81 MPa by substitutional solid solution strengthening across every Ti-1Fe(F) sample. While prior discussions of similar microstructures by Liu et al.[17], and Sandlöbes et al. [16] have inferred a significant solid solution strengthening contribution from Fe in similar microstructures, the present analysis suggests that the direct strengthening effect of Fe is, in fact, negligible from a theoretical standpoint. It is likely that these studies have unintentionally factored the strengthening contributions from the interstitial elements into the contributions for Fe (as O and N have not been treated

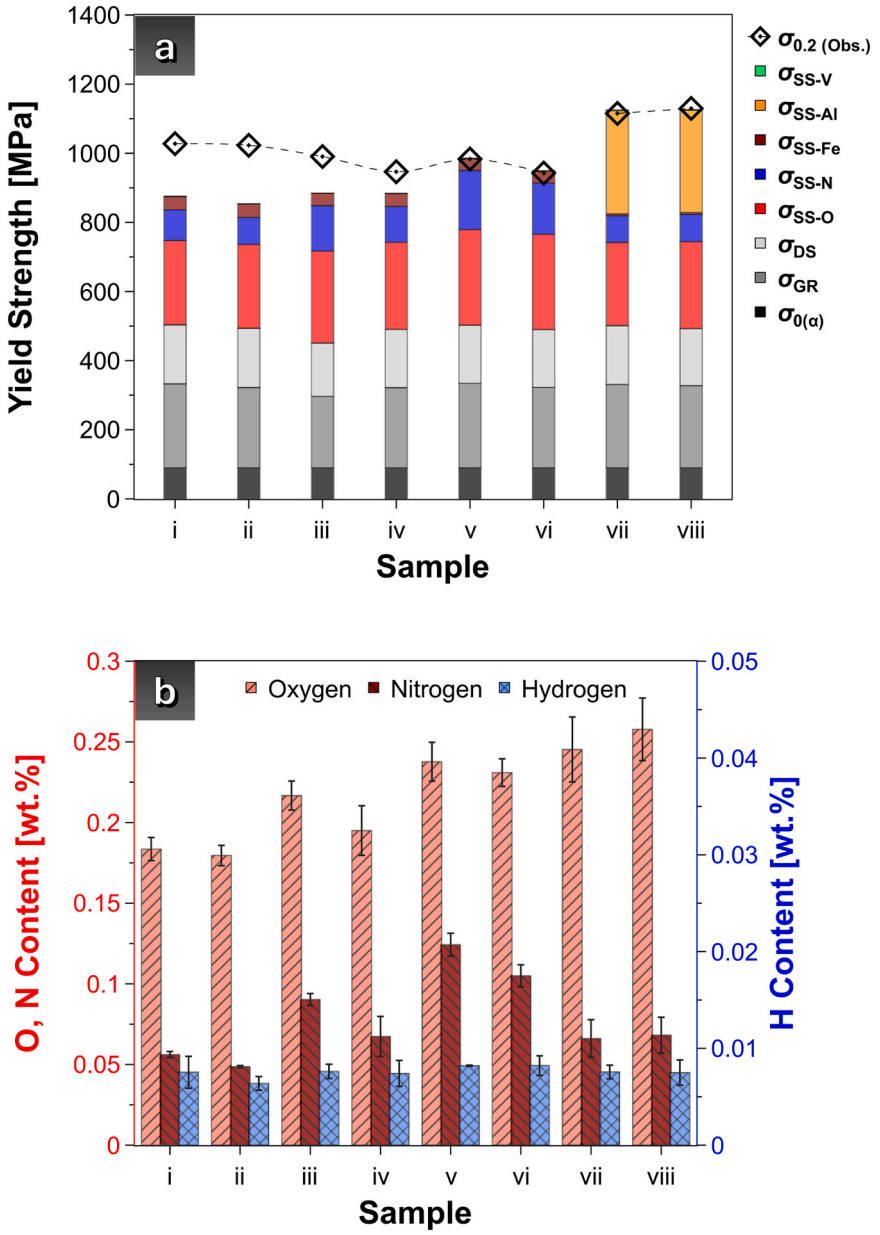


**Fig. 12.** (a) Observed 0.2 % yield strengths and calculated contributions from theoretical strengthening mechanism considered to be active in the α/α' phase. (b) Oxygen, nitrogen and hydrogen content of as-built samples, as evaluated by inert gas fusion. (i-viii) refer to Ti-1Fe(S) built at (i) 60-S, (ii) 60-W, (iii) 120-S, (iv) 120-W, (v) 180-S, (vi) 180-W, and Ti-6Al-4V built at (vii) 120-S and (viii) 120-W.

separately in their methodologies). A low contribution for Fe solid solution strengthening is more physically realistic when considering the low atomic concentration of Fe in the current materials system (1 wt% corresponds to approx. 0.86 at%), as well as the minimal lattice distortion observed in the α/α′ phase relative to ideal Ti lattice parameters, as evidenced by XRD analysis (see Fig. 9 and section 3.3).

However, despite its limited direct contribution to solid solution strengthening, Fe appears to play a critical indirect role in promoting and stabilising the highly refined martensitic grain structure observed in the present material (average lath thickness ~1.5 μm). This microstructural refinement is likely a key factor contributing to the substantial strength enhancement relative to commercially pure titanium (CP-Ti), which typically exhibits much coarser columnar α grains (average widths >100 μm) and significantly lower strength values [60]. Similar grain refinement effects have been reported for interstitial solutes, which promote the formation of fine lath martensite structures [25]. However, in clear contrast to these studies, the addition of Fe appears to uniquely stabilise the thicknesses of the resulting laths with respect to the interstitial content.

As seen in Table 5, the average lath thicknesses in the in-situ alloyed Ti-1Fe remains relatively constant with thicknesses of ~1.5 μm throughout the various build conditions, despite the larger variations in O and N content with the $E_L$), which contrasts the wide range of microstructures observed in PBF-LB/M/CP-Ti with elevated O/N content. Thus, it would appear that small amounts of Fe solutes may potentially contribute towards stabilisation of the grain refinement mechanism across a wider range of the interstitial contents; producing laths of similar scale to Ti-6Al-4V prepared under similar PBF-LB/M conditions (and similar theoretical strengthening contributions of ~230–240 MPa).

Unfortunately, due to the complex interplay between interstitial and substitutional solutes under the non-equilibrium conditions of PBF-LB/M processing, it is not practically feasible to design a control experiment that directly isolates the individual contribution of each element to grain refinement. As discussed in Section 3.3, the microstructures

**Table 4**
Parameters used in the preparation of the strengthening model.

| Parameter / Variable | Symbol | Value | Unit | Notes / Source |
|---|---|---|---|---|
| Lattice Friction of α-Ti | $\sigma_0$ | 90 | MPa | CRSS of Prismatic Slip System [66] |
| Hall-Petch Coefficient of α-Ti | $k_Y$ | 300 | MPa.μ $m^{-1/2}$ | Lath width basis (non-colony) [70] |
| Dislocation Strengthening Coefficient | $\alpha$ | 0.2 | - | [75] |
| Solution Strengthening Parameter, O in α-Ti | $B_O$ | 9068 | MPa. $at^{2/3}$ | *[60,72] |
| Solution Strengthening Parameter, N in α-Ti | $B_N$ | 9284 | MPa. $at^{2/3}$ | *[59,72] |
| Solution Strengthening Parameter, Fe in α-Ti | $B_{Fe}$ | 1985 | MPa. $at^{2/3}$ | *[73] |
| Solution Strengthening Parameter, V in α-Ti | $B_{Al}$ | 1813 | MPa. $at^{2/3}$ | [70] |
| Solution Strengthening Parameter, Al in α-Ti | $B_V$ | 127 | MPa. $at^{2/3}$ | [70] |

*Source reports solution strengthening parameter in Schmid factor basis, these values have been converted to Taylor factor basis using the average Schmid factor (0.37) reported in the original study

present in these materials predominantly arise from a martensitic β → α' transformation, with a small degree of auto-tempering from heat accumulation across subsequent layers. Thus, the elimination or substantial alteration of O, N or Fe concentrations in pursuit of a control sample would completely alter the kinetics of grain formation. Nonetheless, more carefully controlled fundamental investigations into these compositions would certainly be interesting as future work.

## 4. Conclusions

In situ alloyed Ti-1Fe (wt%) prepared from elemental powders was systematically investigated for its potential as a sustainable and low-cost alternative to pre-alloyed Ti-6Al-4V for PBF-LB/M; with attention to the previously unexplored issues of feedstock characteristics, building parameters, and their corresponding influences on as-built microstructures, defect structures, and tensile properties. The novel findings from this work are as follows:

(1) Finer Fe powders, and higher linear energy density input were found to be important pre-requisites for obtaining homogeneous in-situ alloying. Heterogeneities arising from insufficient mixing and dispersion of Fe results in local enrichment beyond the critical concentration required to retain-β on quenching, producing distinct crescent-shaped quasi-β-fleck defects, which have never been reported in similar near-α compositions.
(2) In the samples built from fine (3–8 μm) Fe powders, build parameters were found to have a strong effect on pore formation, Fe homogenisation and microstructure. Lower energy densities resulted in more lack-of-fusion defects, and more Fe segregation, leading to a higher fraction of retained-β. Meanwhile, prior-β grains solidified with a more refined and more randomly oriented texture, which transformed into shorter and more randomly oriented α/α' laths. Conversely, higher energy densities produced more keyhole pores, and more homogeneous microstructures of long α/α' laths arranged in prior-β grains with strong $\{001\}_\beta \,||\, Z$ texture.
(3) Ti-1Fe alloys prepared from 3 to 8 μm Fe powder at higher volumetric energy densities are found to be almost identical Ti-6Al-4V in terms of microstructural morphology and texture. Similarly, the mechanical properties of these samples satisfy the ASTM requirements for PBF-LB/M Ti-6Al-4V, with yield strengths exceeding 900 MPa, tensile strengths greater than 1000 MPa and fracture strains greater than 10 %. Meanwhile, similarly prepared Ti-6Al-4V is still found to be about 200 MPa stronger, however this does not detract from the remarkable performance of the much leaner composition.
(4) A systematic breakdown of theoretical strengthening mechanisms reveals grain boundary strengthening, dislocation strengthening and solid solution strengthening from O/N as significant contributors to the high performance of PBF-LB/M Ti-1Fe, all of which are strongly related to the PBF-LB/M process. In-process O/N pickup is found to partially compensate for the loss of Al solid-solution-strengthening, notably with no detriment to ductility.

Overall, in terms of uniaxial tensile performance, in-situ alloyed Ti-1Fe(F), in the as-built condition is found to be a potentially attractive substitute for Ti-6Al-4V due to the elimination of vanadium (a rare and critical element) in the cheaper and leaner composition. While further investigations into heat-treatability (including stress-reliefs), fatigue, anisotropic effects, residual stresses, and surface properties, and corrosion behaviour will be necessary to justify real-world implementation of such materials, our novel findings provide justification, and a strong foundation for these follow-up studies.

Furthermore, the observed strengthening of titanium by cheap and common impurities (Fe, O and N) with no detriment to ductility appears to warrant the development of new grades of titanium beyond the current specifications of CP-Ti as scrap-compatible compositions for PBF-

**Table 5**
Experimentally derived variables and resulting strengthening contributions.

| Variable (Source) [Unit] | Sample Average Value (Calculated Strengthening Contribution in MPa) | | | | | | | |
|---|---|---|---|---|---|---|---|---|
| | Ti-1Fe(F) | | | | | | Ti-6Al-4V | |
| | 60-S | 60-W | 120-S | 120-W | 180-S | 180-W | 120-S | 180-W |
| α/α' Lath Width (EBSD) [μm] | 1.52 (243) | 1.66 (232) | 2.10 (207) | 1.67 (232) | 1.50 (245) | 1.66 (233) | 1.55 (241) | 1.59 (238) |
| Dislocation Density (EBSD*)[$10^{12}$ $m^{-2}$] | 758 (170) | 763 (171) | 619 (154) | 742 (169) | 735 (168) | 730 (167) | 757 (170) | 713 (165) |
| O Concentration (IGF) [wt%†] | 0.18 (244) | 0.17 (243) | 0.21 (266) | 0.20 (252) | 0.24 (277) | 0.23 (276) | 0.25 (241) | 0.26 (251) |
| N Concentration (IGF) [wt%†] | 0.06 (88) | 0.05 (78) | 0.09 (131) | 0.07 (103) | 0.12 (171) | 0.10 (148) | 0.07 (77) | 0.07 (78) |
| Fe Concentration (ICP-OES) [wt%†] | 1.069 (41.66) | 1.063 (42.09) | 0.995 (35.90) | 1.114 (42.14) | 0.949 (32.45) | 1.020 (35.73) | 0.179 (5.147) | 0.176 (5.056) |
| V Concentration (ICP-OES) [wt%†] | - | - | - | - | - | - | 4.059 (2.068) | 4.144 (2.107) |
| Al Concentration (ICP-OES) [wt%†] | - | - | - | - | - | - | 5.843 (303.4) | 5.665 (293.6) |

*Geometrically necessary dislocations calculated from local misorientations [74]
†wt% concentrations are converted to at% in Labusch model calculations (assuming the balance is pure Ti)

LB/M. To this end, there will be great interest in further fundamental studies dedicated towards the precise explanation of the individual influences of these impurity elements on the physical metallurgy of AM Ti alloys. The present work has attempted to phenomenologically explain the contributions of each key element (O, N, Fe) in connection with accepted solid-solution-strengthening theory, however, the heuristic approach and focus on feedstock and build parameter optimisation is naturally insufficient for explaining precise composition effects on microstructure development. Final microstructures appear to be quite clearly martensitic in nature, but the exact influences of O, N, and Fe on the transformation and grain refinement kinetics will require more controlled experimentation to de-convolute.

In totality, we have empirically demonstrated the possibility of achieving simultaneous strength and ductility in materials near-purity Ti with approximately double the Fe and N content of Grade 4 CP-Ti. Based on these findings, we recommend the continued development of such compositions (and their recycling and supply chains) for additive manufacturing, as a means to improve the sustainability of Ti and lower the cost barrier of the traditionally expensive material.

## CRediT authorship contribution statement

**Kondoh Katsuyoshi:** Writing – review & editing, Supervision, Methodology, Funding acquisition, Conceptualization. **Umeda Junko:** Supervision, Project administration. **Issariyapat Ammarueda:** Writing – review & editing, Methodology. **Kariya Shota:** Validation, Methodology. **Huang Jeff:** Writing – original draft, Visualization, Project administration, Methodology, Investigation, Formal analysis, Conceptualization.

## Declaration of Competing Interest

The authors declare that they have no known competing financial interests or personal relationships that could have appeared to influence the work reported in this paper.

## Acknowledgements

The authors acknowledge funding from the Fund Program for Creating Research-Based Startups from Academia of the Japan Science and Technology Agency (Grant No. JPMJSF23DA), the Environment Research and Technology Development Fund of the Environmental Restoration and Conservation Agency, provided by the Ministry of the Environment (Japan) (Grant No. JPMEERF20213G02), the Project on Design & Engineering by Joint Inverse Innovation for Materials Architecture (DEJI2MA) from the Ministry of Education (Japan), the OU Master Plan Implementation Project of the University of Osaka, and the Light Metal Education Foundation (Japan). The authors would also like to acknowledge Dr. Takeshi Hirano and the Research Fabrication Support Division of the University of Osaka Core Facility Centre for assistance in performing the ICP-OES analysis.

## Appendix A. Supporting information

Supplementary data associated with this article can be found in the online version at doi:10.1016/j.addma.2025.104788.

## Data Availability

Data will be made available on request.

## References

[1] B. Blakey-Milner, P. Gradl, G. Snedden, M. Brooks, J. Pitot, E. Lopez, M. Leary, F. Berto, A. Du Plessis, Metal additive manufacturing in aerospace: a review, Mater. Des. 209 (2021) 110008, https://doi.org/10.1016/j.matdes.2021.110008.

[2] V. Madhavadas, D. Srivastava, U. Chadha, S. Aravind Raj, M.T.H. Sultan, F. S. Shahar, A.U.M. Shah, A review on metal additive manufacturing for intricately shaped aerospace components, CIRP J. Manuf. Sci. Technol. 39 (2022) 18–36, https://doi.org/10.1016/j.cirpj.2022.07.005.

[3] G. Lütjering, Influence of processing on microstructure and mechanical properties of (α+β) titanium alloys, Mater. Sci. Eng.: A 243 (1998) 32–45, https://doi.org/10.1016/S0921-5093(97)00778-8.

[4] T. DebRoy, H.L. Wei, J.S. Zuback, T. Mukherjee, J.W. Elmer, J.O. Milewski, A. M. Beese, A. Wilson-Heid, A. De, W. Zhang, Additive manufacturing of metallic components – process, structure and properties, Prog. Mater. Sci. 92 (2018) 112–224, https://doi.org/10.1016/j.pmatsci.2017.10.001.

[5] B. Vrancken, L. Thijs, J.-P. Kruth, J. Van Humbeeck, Heat treatment of Ti6Al4V produced by Selective Laser Melting: Microstructure and mechanical properties, J. Alloy. Compd. 541 (2012) 177–185, https://doi.org/10.1016/j.jallcom.2012.07.022.

[6] W. Xu, E.W. Lui, A. Pateras, M. Qian, M. Brandt, In situ tailoring microstructure in additively manufactured Ti-6Al-4V for superior mechanical performance, Acta Mater. 125 (2017) 390–400, https://doi.org/10.1016/j.actamat.2016.12.027.

[7] F42 Committee, Specification for Additive Manufacturing Titanium-6 Aluminum-4 Vanadium with Powder Bed Fusion, ASTM International, n.d. https://doi.org/10.1520/F2924–14.

[8] H. Nakajima, M. Koiwa, Diffusion in Titanium, ISIJ Int. 31 (1991) 757–766, https://doi.org/10.2355/isijinternational.31.757.

[9] M. Bignon, E. Bertrand, P.E.J. Rivera-Díaz-del-Castillo, F. Tancret, Martensite formation in titanium alloys: crystallographic and compositional effects, J. Alloy. Compd. 872 (2021) 159636, https://doi.org/10.1016/j.jallcom.2021.159636.

[10] P.J. Bania, Beta titanium alloys and their role in the titanium industry, JOM 46 (1994) 16–19, https://doi.org/10.1007/BF03220742.

[11] M. Koike, C. Ohkubo, H. Sato, H. Fujii, T. Okabe, Evaluation of cast Ti–Fe–O–N alloys for dental applications, Mater. Sci. Eng.: C 25 (2005) 349–356, https://doi.org/10.1016/j.msec.2005.04.002.

[12] N.R. Rundora, J.W. Van Der Merwe, D.E.P. Klenam, M.O. Bodunrin, Enhanced corrosion performance of low-cost titanium alloys in a simulated diabetic environment, Mater. Corros. 74 (2023) 1486–1498, https://doi.org/10.1002/maco.202313927.

[13] O. Takeda, T. Ouchi, T.H. Okabe, Recent progress in titanium extraction and recycling, Met. Mater. Trans. B 51 (2020) 1315–1328, https://doi.org/10.1007/s11663-020-01898-6.

[14] D. Raabe, The materials science behind sustainable metals and alloys, Chem. Rev. 123 (2023) 2436–2608, https://doi.org/10.1021/acs.chemrev.2c00799.

[15] T. Song, Z. Chen, X. Cui, S. Lu, H. Chen, H. Wang, T. Dong, B. Qin, K.C. Chan, M. Brandt, X. Liao, S.P. Ringer, M. Qian, Strong and ductile titanium–oxygen–iron alloys by additive manufacturing, Nature 618 (2023) 63–68, https://doi.org/10.1038/s41586-023-05952-6.

[16] S. Sandlöbes, S. Korte-Kerzel, D. Raabe, On the influence of the heat treatment on microstructure formation and mechanical properties of near-α Ti-Fe alloys, Mater. Sci. Eng.: A 748 (2019) 301–312, https://doi.org/10.1016/j.msea.2018.12.071.

[17] C. Liu, J. Chen, Y. Wang, W. Ding, Q. Tao, G. Chen, W. Cai, M. Qin, X. Qu, Strong and ductile nanoscale Ti-1Fe dual-phase alloy via deformation twinning, Scr. Mater. 237 (2023) 115720, https://doi.org/10.1016/j.scriptamat.2023.115720.

[18] L. Mugwagwa, D. Dimitrov, S. Matope, I. Yadroitsev, Evaluation of the impact of scanning strategies on residual stresses in selective laser melting, Int J. Adv. Manuf. Technol. 102 (2019) 2441–2450, https://doi.org/10.1007/s00170-019-03396-9.

[19] J. Gostick, Z. Khan, T. Tranter, M. Kok, M. Agnaou, M. Sadeghi, R. Jervis, PoreSpy: a python toolkit for quantitative analysis of porous media images, JOSS 4 (2019) 1296, https://doi.org/10.21105/joss.01296.

[20] B.L. Adams, S.I. Wright, K. Kunze, Orientation imaging: the emergence of a new microscopy, Met. Trans. A 24 (1993) 819–831, https://doi.org/10.1007/BF02656503.

[21] W.G. Burgers, On the process of transition of the cubic-body-centered modification into the hexagonal-close-packed modification of zirconium, Physica 1 (1934) 561–586, https://doi.org/10.1016/S0031-8914(34)80244-3.

[22] S.I. Wright, W.C. Lenthe, M.M. Nowell, Parent grain reconstruction in an additive manufactured titanium alloy, Metals 14 (2023) 51, https://doi.org/10.3390/met14010051.

[23] N. Doebelin, R. Kleeberg, *Profex*: a graphical user interface for the Rietveld refinement program BGMN, J. Appl. Crystallogr. 48 (2015) 1573–1580, https://doi.org/10.1107/S1600576715014685.

[24] S. Gražulis, D. Chateigner, R.T. Downs, A.F.T. Yokochi, M. Quirós, L. Lutterotti, E. Manakova, J. Butkus, P. Moeck, A. Le Bail, Crystallography open database – an open-access collection of crystal structures, J. Appl. Crystallogr 42 (2009) 726–729, https://doi.org/10.1107/S0021889809016690.

[25] A. Issariyapat, S. Kariya, K. Shitara, J. Umeda, K. Kondoh, Solute-induced near-isotropic performance of laser powder bed fusion manufactured pure titanium, Addit. Manuf. 56 (2022) 102907, https://doi.org/10.1016/j.addma.2022.102907.

[26] DIN EN ISO 6892–1:2020–06, Metallische Werkstoffe_- Zugversuch_- Teil_1: Prüfverfahren bei Raumtemperatur (ISO_6892–1:2019); Deutsche Fassung EN_ISO_6892–1:2019, (n.d.).http://doi.org/10.31030/3132591

[27] M.S. Knieps, W.J. Reynolds, J. Dejaune, A.T. Clare, A. Evirgen, In-situ alloying in powder bed fusion: the role of powder morphology, Mater. Sci. Eng.: A 807 (2021) 140849, https://doi.org/10.1016/j.msea.2021.140849.

[28] I. Yadroitsev, P. Krakhmalev, I. Yadroitsava, Titanium alloys manufactured by in situ alloying during laser powder bed fusion, JOM 69 (2017) 2725–2730, https://doi.org/10.1007/s11837-017-2600-7.

[29] M. Simonelli, N.T. Aboulkhair, P. Cohen, J.W. Murray, A.T. Clare, C. Tuck, R.J. M. Hague, A comparison of Ti-6Al-4V in-situ alloying in Selective Laser Melting

using simply-mixed and satellited powder blend feedstocks, Mater. Charact. 143 (2018) 118–126, https://doi.org/10.1016/j.matchar.2018.05.039.
[30] H. Li, E.G. Brodie, C. Hutchinson, Predicting the chemical homogeneity in laser powder bed fusion (LPBF) of mixed powders after remelting, Addit. Manuf. 65 (2023) 103447, https://doi.org/10.1016/j.addma.2023.103447.
[31] N. Kang, X. Lin, C. Coddet, X. Wen, W. Huang, Selective laser melting of low modulus Ti-Mo alloy: α/β heterogeneous conchoidal structure, Mater. Lett. 267 (2020) 127544, https://doi.org/10.1016/j.matlet.2020.127544.
[32] A. Mitchell, A. Kawakami, S.L. Cockcroft, Beta fleck and segregation in titanium alloy ingots, High. Temp. Mater. Process. 25 (2006) 337–349, https://doi.org/10.1515/HTMP.2006.25.5-6.337.
[33] H. Azizi, H. Zurob, B. Bose, S. Reza Ghiaasiaan, X. Wang, S. Coulson, V. Duz, A. B. Phillion, Additive manufacturing of a novel Ti-Al-V-Fe alloy using selective laser melting, Addit. Manuf. 21 (2018) 529–535, https://doi.org/10.1016/j.addma.2018.04.006.
[34] J. Umeda, T. Tanaka, T. Teramae, S. Kariya, J. Fujita, H. Nishikawa, Y. Shibutani, J. Shen, K. Kondoh, Microstructures analysis and quantitative strengthening evaluation of powder metallurgy Ti–Fe binary extruded alloys with (α+β)-dual-phase, Mater. Sci. Eng.: A 803 (2021) 140708, https://doi.org/10.1016/j.msea.2020.140708.
[35] T. DebRoy, S.A. David, Physical processes in fusion welding, Rev. Mod. Phys. 67 (1995) 85–112, https://doi.org/10.1103/RevModPhys.67.85.
[36] W.E. King, H.D. Barth, V.M. Castillo, G.F. Gallegos, J.W. Gibbs, D.E. Hahn, C. Kamath, A.M. Rubenchik, Observation of keyhole-mode laser melting in laser powder-bed fusion additive manufacturing, J. Mater. Process. Technol. 214 (2014) 2915–2925, https://doi.org/10.1016/j.jmatprotec.2014.06.005.
[37] Y. Huang, T.G. Fleming, S.J. Clark, S. Marussi, K. Fezzaa, J. Thiyagalingam, C.L. A. Leung, P.D. Lee, Keyhole fluctuation and pore formation mechanisms during laser powder bed fusion additive manufacturing, Nat. Commun. 13 (2022) 1170, https://doi.org/10.1038/s41467-022-28694-x.
[38] T. Voisin, N.P. Calta, S.A. Khairallah, J.-B. Forien, L. Balogh, R.W. Cunningham, A. D. Rollett, Y.M. Wang, Defects-dictated tensile properties of selective laser melted Ti-6Al-4V, Mater. Des. 158 (2018) 113–126, https://doi.org/10.1016/j.matdes.2018.08.004.
[39] Q. Luo, L. Yin, T.W. Simpson, A.M. Beese, Effect of processing parameters on pore structures, grain features, and mechanical properties in Ti-6Al-4V by laser powder bed fusion, Addit. Manuf. 56 (2022) 102915, https://doi.org/10.1016/j.addma.2022.102915.
[40] W.H. Kan, L.N.S. Chiu, C.V.S. Lim, Y. Zhu, Y. Tian, D. Jiang, A. Huang, A critical review on the effects of process-induced porosity on the mechanical properties of alloys fabricated by laser powder bed fusion, J. Mater. Sci. 57 (2022) 9818–9865, https://doi.org/10.1007/s10853-022-06990-7.
[41] J. Yang, H. Yu, J. Yin, M. Gao, Z. Wang, X. Zeng, Formation and control of martensite in Ti-6Al-4V alloy produced by selective laser melting, Mater. Des. 108 (2016) 308–318, https://doi.org/10.1016/j.matdes.2016.06.117.
[42] S.L. Lu, C.J. Todaro, Y.Y. Sun, T. Song, M. Brandt, M. Qian, Variant selection in additively manufactured alpha-beta titanium alloys, J. Mater. Sci. Technol. 113 (2022) 14–21, https://doi.org/10.1016/j.jmst.2021.10.021.
[43] S.C. Wang, M. Aindow, M.J. Starink, Effect of self-accommodation on α/α boundary populations in pure titanium, Acta Mater. 51 (2003) 2485–2503, https://doi.org/10.1016/S1359-6454(03)00035-1.
[44] A. Basak, S. Das, Epitaxy and microstructure evolution in metal additive manufacturing, Annu. Rev. Mater. Res. 46 (2016) 125–149, https://doi.org/10.1146/annurev-matsci-070115-031728.
[45] D. Zhang, D. Qiu, M.A. Gibson, Y. Zheng, H.L. Fraser, D.H. StJohn, M.A. Easton, Additive manufacturing of ultrafine-grained high-strength titanium alloys, Nature 576 (2019) 91–95, https://doi.org/10.1038/s41586-019-1783-1.
[46] G.M. Ter Haar, T.H. Becker, The influence of microstructural texture and prior beta grain recrystallisation on the deformation behaviour of laser powder bed fusion produced Ti–6Al–4V, Mater. Sci. Eng.: A 814 (2021) 141185, https://doi.org/10.1016/j.msea.2021.141185.
[47] J. Peterson, S. Kariya, A. Issariyapat, J. Umeda, K. Kondoh, Experimentally mapping the oriented-to-misoriented transition in laser powder bed fusion Ti-10% Mo alloys, Scr. Mater. 231 (2023) 115472, https://doi.org/10.1016/j.scriptamat.2023.115472.
[48] M. Simonelli, D.G. McCartney, P. Barriobero-Vila, N.T. Aboulkhair, Y.Y. Tse, A. Clare, R. Hague, The influence of iron in minimizing the microstructural anisotropy of Ti-6Al-4V produced by laser powder-bed fusion, Met. Mater. Trans. A 51 (2020) 2444–2459, https://doi.org/10.1007/s11661-020-05692-6.
[49] T. Vilaro, C. Colin, J.D. Bartout, As-fabricated and heat-treated microstructures of the Ti-6Al-4V alloy processed by selective laser melting, Met. Mat. Trans. A 42 (2011) 3190–3199, https://doi.org/10.1007/s11661-011-0731-y.
[50] S. Leuders, M. Thöne, A. Riemer, T. Niendorf, T. Tröster, H.A. Richard, H.J. Maier, On the mechanical behaviour of titanium alloy TiAl6V4 manufactured by selective laser melting: Fatigue resistance and crack growth performance, Int. J. Fatigue 48 (2013) 300–307, https://doi.org/10.1016/j.ijfatigue.2012.11.011.
[51] S. Leuders, T. Lieneke, S. Lammers, T. Tröster, T. Niendorf, On the fatigue properties of metals manufactured by selective laser melting – the role of ductility, J. Mater. Res. 29 (2014) 1911–1919, https://doi.org/10.1557/jmr.2014.157.
[52] M. Simonelli, Y.Y. Tse, C. Tuck, Effect of the build orientation on the mechanical properties and fracture modes of SLM Ti–6Al–4V, Mater. Sci. Eng.: A 616 (2014) 1–11, https://doi.org/10.1016/j.msea.2014.07.086.
[53] W. Xu, M. Brandt, S. Sun, J. Elambasseril, Q. Liu, K. Latham, K. Xia, M. Qian, Additive manufacturing of strong and ductile Ti–6Al–4V by selective laser melting via in situ martensite decomposition, Acta Mater. 85 (2015) 74–84, https://doi.org/10.1016/j.actamat.2014.11.028.
[54] S. Cao, Z. Chen, C.V.S. Lim, K. Yang, Q. Jia, T. Jarvis, D. Tomus, X. Wu, Defect, microstructure, and mechanical property of Ti-6Al-4V alloy fabricated by high-power selective laser melting, JOM 69 (2017) 2684–2692, https://doi.org/10.1007/s11837-017-2581-6.
[55] Y. Yang, Y.J. liu, J. Chen, H.L. Wang, Z.Q. Zhang, Y.J. Lu, S.Q. Wu, J.X. Lin, Crystallographic features of α variants and β phase for Ti-6Al-4V alloy fabricated by selective laser melting, Mater. Sci. Eng.: A 707 (2017) 548–558, https://doi.org/10.1016/j.msea.2017.09.068.
[56] S. Cao, R. Chu, X. Zhou, K. Yang, Q. Jia, C.V.S. Lim, A. Huang, X. Wu, Role of martensite decomposition in tensile properties of selective laser melted Ti-6Al-4V, J. Alloy. Compd. 744 (2018) 357–363, https://doi.org/10.1016/j.jallcom.2018.02.111.
[57] X. Shi, C. Yan, W. Feng, Y. Zhang, Z. Leng, Effect of high layer thickness on surface quality and defect behavior of Ti-6Al-4V fabricated by selective laser melting, Opt. Laser Technol. 132 (2020) 106471, https://doi.org/10.1016/j.optlastec.2020.106471.
[58] S. Sun, D. Zhang, S. Palanisamy, Q. Liu, M.S. Dargusch, Mechanical properties and deformation mechanisms of martensitic Ti6Al4V alloy processed by laser powder bed fusion and water quenching, Mater. Sci. Eng.: A 839 (2022) 142817, https://doi.org/10.1016/j.msea.2022.142817.
[59] A. Issariyapat, P. Visuttipitukul, J. Umeda, K. Kondoh, Refined grain formation behavior and strengthening mechanism of α-titanium with nitrogen fabricated by selective laser melting, Addit. Manuf. 36 (2020) 101537, https://doi.org/10.1016/j.addma.2020.101537.
[60] K. Kondoh, E. Ichikawa, A. Issariyapat, K. Shitara, J. Umeda, B. Chen, S. Li, Tensile property enhancement by oxygen solutes in selectively laser melted titanium materials fabricated from pre-mixed pure Ti and TiO2 powder, Mater. Sci. Eng.: A 795 (2020) 139983, https://doi.org/10.1016/j.msea.2020.139983.
[61] M.T. Hasib, H.E. Ostergaard, Q. Liu, X. Li, J.J. Kruzic, Tensile and fatigue crack growth behavior of commercially pure titanium produced by laser powder bed fusion additive manufacturing, Addit. Manuf. 45 (2021) 102027, https://doi.org/10.1016/j.addma.2021.102027.
[62] F. Haase, C. Siemers, J. Rösler, Laser powder bed fusion (LPBF) of commercially pure titanium and alloy development for the LPBF process, Front. Bioeng. Biotechnol. 11 (2023) 1260925, https://doi.org/10.3389/fbioe.2023.1260925.
[63] F.N. Depboylu, E. Yasa, O. Poyraz, F. Korkusuz, Thin-walled commercially pure titanium structures: laser powder bed fusion process parameter optimization, Machines 11 (2023) 272, https://doi.org/10.3390/machines11020272.
[64] F04 Committee, Specification for Wrought Titanium-6Aluminum-4Vanadium Alloy for Surgical Implant Applications (UNS R56400), ASTM International, n.d. http://doi.org/10.1520/F1472-14
[65] J. Nakahigashi, K. Takahata, K. Tsuru, T. Sumimoto, H. Yoshimura, H. Horimura, Ultra-fine grain refinement of titanium materials by hydrogen treatment (in Japanese), J. Jpn. Inst. Met. 70 (2006) 204–211, https://doi.org/10.2320/jinstmet.70.204.
[66] A.T. Churchman, The slip modes of titanium and the effect of purity on their occurrence during tensile deformation of single crystals, Proc. R. Soc. Lond. A 226 (1954) 216–226, https://doi.org/10.1098/rspa.1954.0250.
[67] R. Labusch, A Statistical Theory of Solid Solution Hardening, Phys. Status Solidi (b) 41 (1970) 659–669, https://doi.org/10.1002/pssb.19700410221.
[68] L.A. Gypen, A. Deruyttere, Multi-component solid solution hardening: part 1 proposed model, J. Mater. Sci. 12 (1977) 1028–1033, https://doi.org/10.1007/BF00540987.
[69] I. Toda-Caraballo, P.E.J. Rivera-Díaz-del-Castillo, Modelling solid solution hardening in high entropy alloys, Acta Mater. 85 (2015) 14–23, https://doi.org/10.1016/j.actamat.2014.11.014.
[70] M.A. Galindo-Fernández, K. Mumtaz, P.E.J. Rivera-Díaz-del-Castillo, E.I. Galindo-Nava, H. Ghadbeigi, A microstructure sensitive model for deformation of Ti-6Al-4V describing cast-and-wrought and additive manufacturing morphologies, Mater. Des. 160 (2018) 350–362, https://doi.org/10.1016/j.matdes.2018.09.028.
[71] R.I. Jaffee, The physical metallurgy of titanium alloys, Prog. Met. Phys. 7 (1958) 65–163, https://doi.org/10.1016/0502-8205(58)90004-2.
[72] A. Issariyapat, J. Huang, T. Teramae, S. Kariya, A. Bahador, P. Visuttipitukul, J. Umeda, A. Alhazaa, K. Kondoh, Microstructure Refinement and Strengthening Mechanisms of Additively Manufactured Ti-Zr Alloys Prepared From Pre-mixed Feedstock, (2023). https://doi.org/10.1016/j.addma.2023.103649.
[73] S. Kariya, I. Ammarueda, A. Bahador, M. Qian, J. Umeda, K. Kondoh, Microstructure and strengthening mechanism of Fe-supersaturated α titanium alloy produced by laser powder bed fusion (in Japanese), J. Jpn. Soc. Powder Powder Metall. (2024) 23–00068, https://doi.org/10.2497/jjspm.23-00068.
[74] K. Yamanaka, A. Kuroda, M. Ito, M. Mori, H. Bian, T. Shobu, S. Sato, A. Chiba, Quantifying the dislocation structures of additively manufactured Ti–6Al–4V alloys using X-ray diffraction line profile analysis, Addit. Manuf. 37 (2021) 101678, https://doi.org/10.1016/j.addma.2020.101678.
[75] G.S. Dyakonov, S. Mironov, I.P. Semenova, R.Z. Valiev, Strengthening mechanisms and super-strength of severely deformed titanium, in: Nanocrystalline Titanium, Elsevier, 2019, pp. 123–143, https://doi.org/10.1016/B978-0-12-814599-9.00007-9.
[76] D.P. Field, P.B. Trivedi, S.I. Wright, M. Kumar, Analysis of local orientation gradients in deformed single crystals, Ultramicroscopy 103 (2005) 33–39, https://doi.org/10.1016/j.ultramic.2004.11.016.
[77] C. Zeng, H. Wen, H. Bellamy, P.T. Sprunger, P.J. Schilling, S.M. Guo, Titanium and nitrogen interactions under laser additive manufacturing conditions, Surf. Coat. Technol. 378 (2019) 124955, https://doi.org/10.1016/j.surfcoat.2019.124955.
[78] C. Pauzon, K. Dietrich, P. Forêt, S. Dubiez-Le Goff, E. Hryha, G. Witt, Control of residual oxygen of the process atmosphere during laser-powder bed fusion

processing of Ti-6Al-4V, Addit. Manuf. 38 (2021) 101765, https://doi.org/10.1016/j.addma.2020.101765.
[79] F04 Committee, Specification for Unalloyed Titanium, for Surgical Implant Applications (UNS R50250, UNS R50400, UNS R50550, UNS R50700), ASTM International, n.d. https://doi.org/10.1520/F0067-13.
[80] Y. Chong, R. Gholizadeh, T. Tsuru, R. Zhang, K. Inoue, W. Gao, A. Godfrey, M. Mitsuhara, J.W. Morris, A.M. Minor, N. Tsuji, Grain refinement in titanium prevents low temperature oxygen embrittlement, Nat. Commun. 14 (2023) 404, https://doi.org/10.1038/s41467-023-36030-0.
[81] M. Chen, S. Van Petegem, Z. Zou, M. Simonelli, Y.Y. Tse, C.S.T. Chang, M. G. Makowska, D. Ferreira Sanchez, H. Moens-Van Swygenhoven, Microstructural engineering of a dual-phase Ti-Al-V-Fe alloy via in situ alloying during laser powder bed fusion, Addit. Manuf. 59 (2022) 103173, https://doi.org/10.1016/j.addma.2022.103173.